Matter

CellPress
OPEN ACCESS

Article

Extreme mixing in nanoscale transition metal alloys

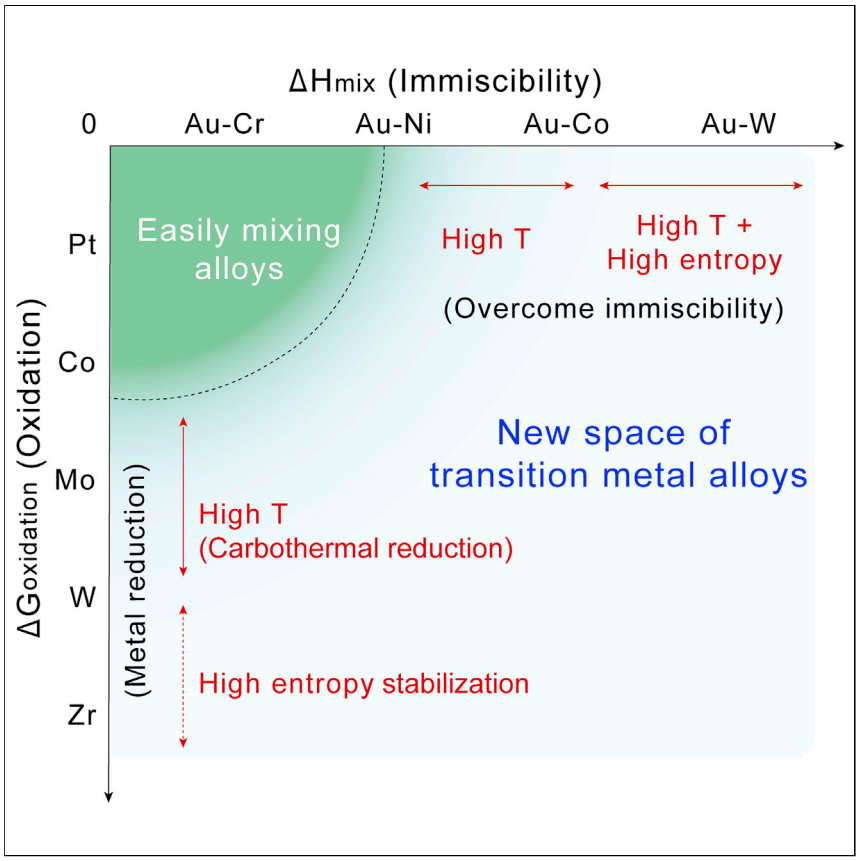

Conventionally, alloys are mostly synthesized in the region of easy mixing, i.e., with light immiscibility and oxidation potentials. Yet such a limited elemental combination largely hinders possible tunability and material discovery. By using entropic design (high temperature and high entropy) that favors uniform mixing, we extended nanoscale alloying to previous unmixable regions by including strongly immiscible and easily oxidized combinations, which we called an extreme mixing. The new alloy space could bring forth exotic nanomaterials for broad applications.

Yonggang Yao, Zhennan Huang, Lauren A. Hughes, ..., Andrew M. Minor, Reza Shahbazian-Yassar, Liangbing Hu

binghu@umd.edu

Highlights

A record 15-element nanoalloy was achieved by extreme entropic design and stabilization

Nanoscale alloys entered into regions featuring strong immiscibility and easy oxidation

Mixing enthalpy and Ellingham diagram can effectively guide the nanoscale alloy design

The first observation of localized strain and lattice distortions in extreme nanoalloys

Benchmark
First qualification/assessment of material properties and/or performance

Yao et al., Matter 4, 2340–2353
July 7, 2021
https://doi.org/10.1016/j.matt.2021.04.014

CellPress
OPEN ACCESS

Matter

Article

Extreme mixing in nanoscale transition metal alloys

Yonggang Yao,[1,11] Zhennan Huang,[2,8] Lauren A. Hughes,[3,4] Jinlong Gao,[1] Tangyuan Li,[1] David Morris,[5] Steven Eric Zeltmann,[3,4] Benjamin H. Savitzky,[4] Colin Ophus,[4] Y. Zou Finfrock,[6,10] Qi Dong,[1] Miaolun Jiao,[1] Yimin Mao,[1,7] Miaofang Chi,[8] Peng Zhang,[5] Ju Li,[9] Andrew M. Minor,[3,4] Reza Shahbazian-Yassar,[2] and Liangbing Hu[1,12,*]

SUMMARY

The ability to alloy different elements is critical for property tuning and materials discovery. However, general alloying at the nanoscale remains extremely challenging due to strong immiscibility and easy oxidation, particularly for early transition metals that are highly reactive. Here, we report nanoscale alloying using a high-temperature- and high-entropy-based strategy ($T^*\Delta S_{mix}$) to significantly expand the possible alloys and include early transition metals. While high-temperature synthesis favors alloy formation and metal reduction, the high-entropy compositional design is critical to further extending the alloying to strongly repelling combinations (e.g., Au-W) and easily oxidized elements (e.g., Zr). In particular, we explicitly characterized a record 15-element nanoalloy, which showed a solid-solution structure featuring localized strain and lattice distortions as a result of extreme mixing. Our study significantly broadens available compositions of nanoalloys and provides clear guidelines by utilizing the less-explored entropic chemistry.

INTRODUCTION

Alloys represent a vast compositional space for material discovery. In particular, transition metal alloys offer largely tunable performances through strong interactions and hybridization of multielement chemistry, which can lead to superior reactivity and selectivity in a range of thermo- and electrocatalysis applications.[1–6] However, considering the wide range of transition metals from group IV to group XI, alloying these largely different elements has proved extremely challenging.[5,7,8] Figure 1A shows the physicochemical differences among transition metals with a wide range of atom sizes, valences, electronegativity, and crystalline structures (see also Table S1), which would lead to immiscibility and failure of alloying. In addition, non-noble transition elements are easily oxidized, particularly for early transition metals that are highly reactive and oxophilic,[1,9] resulting in oxide phases and failure of metallic alloying. For instance, W strongly repels Au, while Zr has a highly negative oxidation potential, and no alloy was reported at nanoscale among these combinations. As previous literature shows, out of the vast potential compositional space for five component systems (e.g., $>10^5$ equal molar compositions), only a few hundred (~200) are single phases as predicted by theoretical calculations,[10–12] demonstrating the scarcity and challenge of uniform alloying.

Traditionally, the Hume-Rothery alloying rule[13] guides bulk alloy formation by limiting the compositions to only similar elements (i.e., atomic size difference [δ]

Progress and potential

New materials with exotic functionalities are most often constructed by alloying. However, such a capability is constrained by elemental or phase immiscibility, which are even exaggerated at nanoscale due to the short diffusion length and easy oxidation. Hume-Rothery rules could guide the alloy design and formation but are largely limited to narrow combinations and bulk scale scenarios. In this work, we proposed the use of extreme entropic driving force—high-temperature (~1,800 K) and high-entropy (15 element) design—to largely extend such an alloy space at nanoscale to include strongly immiscible and easily oxidized combinations. In addition, the mixing enthalpy and Ellingham diagram provide critical guidelines for nanoscale alloy design and prediction. As a result of extreme mixing, we observed localized strain and lattice distortions in these entropy-stabilized nanoalloys. This study opens up a vast space for nanoscale material manipulation and discovery.

of <15%, similar structure, valences, and electronegativity). Quantitatively, density functional theory has predicted ~900 binary metallic combinations and has found a small mixing enthalpy ΔH_{mix} < 37 meV (3.57 kJ/mol) that is a safe upper limit for uniform alloying by data analysis among numerous experimental reports.[10] Similar empirical single-phase selection rules have been established in multielement high-entropy alloys (HEAs), again by restricting the possible alloy elements to a range of approximately −15 kJ/mol < ΔH_{mix} < 5 kJ/mol and 0 < δ < 5%, or similar confinement.[10–12,14–18] As a result, facile alloying is generally found under restricted conditions for elements with a small mixing enthalpy and oxidation potential, as shown in the range within the green line in Figure 1B. Nevertheless, these existing phase selection rules render very limited alloys and largely restricted compositional spaces for material discovery. Moreover, the extremely small short diffusion length for nanoscale particles accelerates potential phase separation, oxidation, and therefore failure of alloying.[7,8,19,20] Consequently, literature reports on extreme mixing (i.e., mixing of previously unmixable elements) for nanoscale alloys beyond existing rules are rare, and there are no clear guidelines on nanoalloy design and synthesis.

Here, we report the systematic study of alloying in an extended spectrum of transition metals with a focus on addressing the immiscibility and oxidation problems that occur in nanoscale alloying. In contrast to the existing rules that restrict alloys among only similar elements, we used a high-temperature- and high-entropy-based strategy ($T^*\Delta S_{mix}$) to drive alloy formation thermodynamically, which is non-specific to alloy compositions and thus enables general alloying (Figure 1B). In addition, the high-temperature synthesis can induce nanoscale metal reduction and avoid oxide impurities. Kinetically, the high-entropy structure features multielement mixing with distorted lattices, which could stabilize those immiscible combinations and reduced elements into entropy-stabilized alloys, featuring extreme mixing alloys that were not previously possible. Here, we denote "extreme mixing" as alloy formation beyond the prediction by existing rules.

As shown in Figure 1C, our study increased the synthesis temperature from regular nanomaterial synthesis at 300–800 K to a high temperature of 1,800 K and the configurational entropy from binary (ΔS_{conf} = 5.76 J/mol/K) to 15-element mixing (ΔS_{conf} = 22.51 J/mol/K), thereby substantially increasing the entropic contribution $T^*\Delta S_{mix}$ by ~8-fold to ~40 kJ/mol, which is critical in counterbalancing the enthalpy penalty and driving alloy formation ($\Delta G_{mix} = \Delta H_{mix} - T^*\Delta S_{mix}$). Based on our synthesis, we demonstrated an extreme mixing of 15 early and late transition metals in a uniform alloy structure, including strongly repelling Au and W, as shown in the element mapping by scanning transmission electron microscopy (STEM) (Figure 1D). Note that Sn is included because it is intensively studied for alloying with transition metals for catalysis and energy applications.[21–23] Therefore, by using the entropic contribution, our study significantly extends the mixing potential of transition metals and acts as a guideline for nanoscale alloy synthesis.

RESULTS

Entropic contribution to overcoming immiscibility

Au-based binary systems with a wide range of mixing enthalpy (calculated by density functional theory,[10] Table S2) were chosen to explore the synthetic boundaries of entropic driving force to overcome immiscibility. For example, Au-Ni has a mixing enthalpy ΔH_{mix} = 4.25 kJ/mol, which is beyond the single-phase alloy rules and shows a large immiscible gap in the phase diagram at low temperature (Figure 2A). This is confirmed by wet chemical synthesis of Au-Ni (and Au-Co) showing clear

[1]Department of Materials Science and Engineering, University of Maryland, College Park, MD 20742, USA

[2]Department of Mechanical and Industrial Engineering, University of Illinois at Chicago, 842 West Taylor Street, Chicago, IL 60607, USA

[3]Department of Materials Science and Engineering, University of California, Berkeley, CA 94720, USA

[4]National Center for Electron Microscopy, Molecular Foundry, Lawrence Berkeley National Laboratory, Berkeley, CA 94720, USA

[5]Department of Chemistry, Dalhousie University, Halifax, NS B3H 4R2, Canada

[6]Science Division, Canadian Light Source Inc., 44 Innovation Boulevard, Saskatoon, SK S7N 2V3, Canada

[7]NIST Center for Neutron Research, National Institute of Standards and Technology, Gaithersburg, MD 20899, USA

[8]Center for Nanophase Materials Sciences, Oak Ridge National Laboratory, Oak Ridge, TN 37831, USA

[9]Department of Nuclear Science and Engineering, Department of Materials Science and Engineering, Massachusetts Institute of Technology, Cambridge, MA 02139, USA

[10]CLS@APS, Sector 20, Advanced Photon Source, Argonne National Laboratory, 9700 Cass Avenue, Lemont, IL 60439, USA

[11]Present address: School of Materials Science and Engineering, State Key Laboratory of Materials Processing and Die & Mold Technology, Huazhong University of Science and Technology, Wuhan 430074, China

[12]Lead contact

*Correspondence: binghu@umd.edu

https://doi.org/10.1016/j.matt.2021.04.014

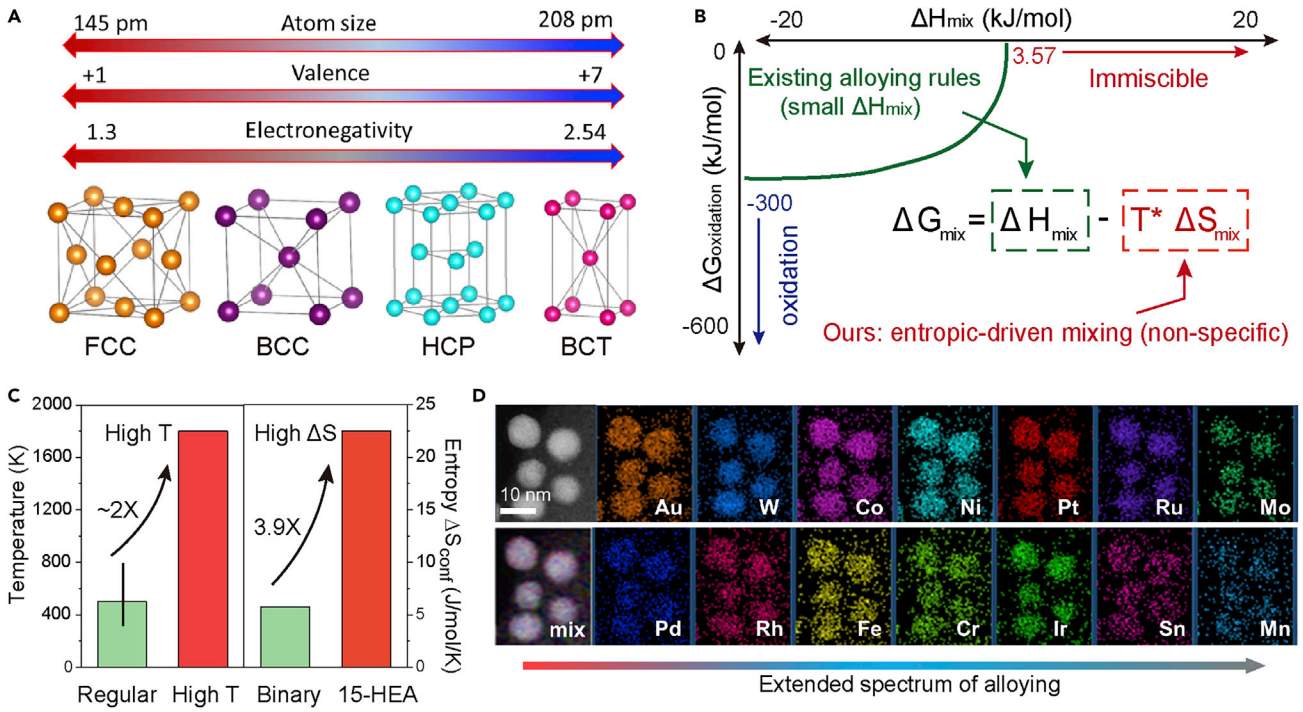

Figure 1. Extreme alloying by a high-temperature and high-entropy synthesis

(A) Transition metal elements and their largely different physiochemical properties.

(B) Existing single-phase alloying rule (a small ΔH_{mix}) and our strategies based on the entropic contribution ($-T\Delta S_{mix}$) to enable more alloy choices.

(C) The high temperature and high entropy (configurational entropy) in this study (1,800 K, 15 element mixing) compared with typical nanomaterial studies (300–800 K, binary systems), rendering an entropic driving force of approximately −40 kJ/mol.

(D) STEM elemental maps of extreme mixing in nanoparticles containing 15 different elements including both late and early transition metals, made possible by the high-temperature and high-entropy synthesis (Cu mapping data is not shown due to use of the Cu grid).

phase separation toward hybrid nanoparticles.[24] However, at high temperatures, Au-Ni can be uniformly mixed owing to the increasing temperature and entropy that drive the alloy formation. Therefore, a rapid high-temperature synthesis could lead to uniform alloy formation whereby the high temperature drives the alloy mixing while the subsequent rapid cooling can help maintain the small size distribution and uniform alloy structure.[18,25–31]

Experimentally, we synthesized AuNi binary alloy nanoparticles on a carbon nanofiber substrate using carbothermal shock synthesis[5] driven by direct Joule heating (e.g., 1,800 K, 50 ms; see experimental procedures and Figure S1). The process is similar to previous non-equilibrium synthesis,[5,32] but this work focuses on discovering and exploring alloying principles and guidelines in transition metal alloys using the less-explored entropic term. In particular, the kinetic quenching (cooling rate on the order of 10^4–10^5 K/s) maximized the possibility of alloy formation by eliminating the possible phase separation during slow cooling. After synthesis, we observed uniform nanoparticles dispersed on the carbon substrate (Figure S2A) and confirmed a face-centered-cubic (FCC) single-phase alloy structure by X-ray diffraction (XRD) (Figure 2B). In comparison, a low-temperature control synthesis (~800 K, 50 ms, repeated three times for a complete reaction) leads to a clear peak splitting in XRD, indicating the importance of high-temperature synthesis (Figure 2B). Using the same high-temperature process, we also synthesized Au-based alloys previously considered immiscible with a range of mixing enthalpy,[10,24] including AuNi, AuFe, and AuCo, which now demonstrate a single-phase structure confirmed by powder

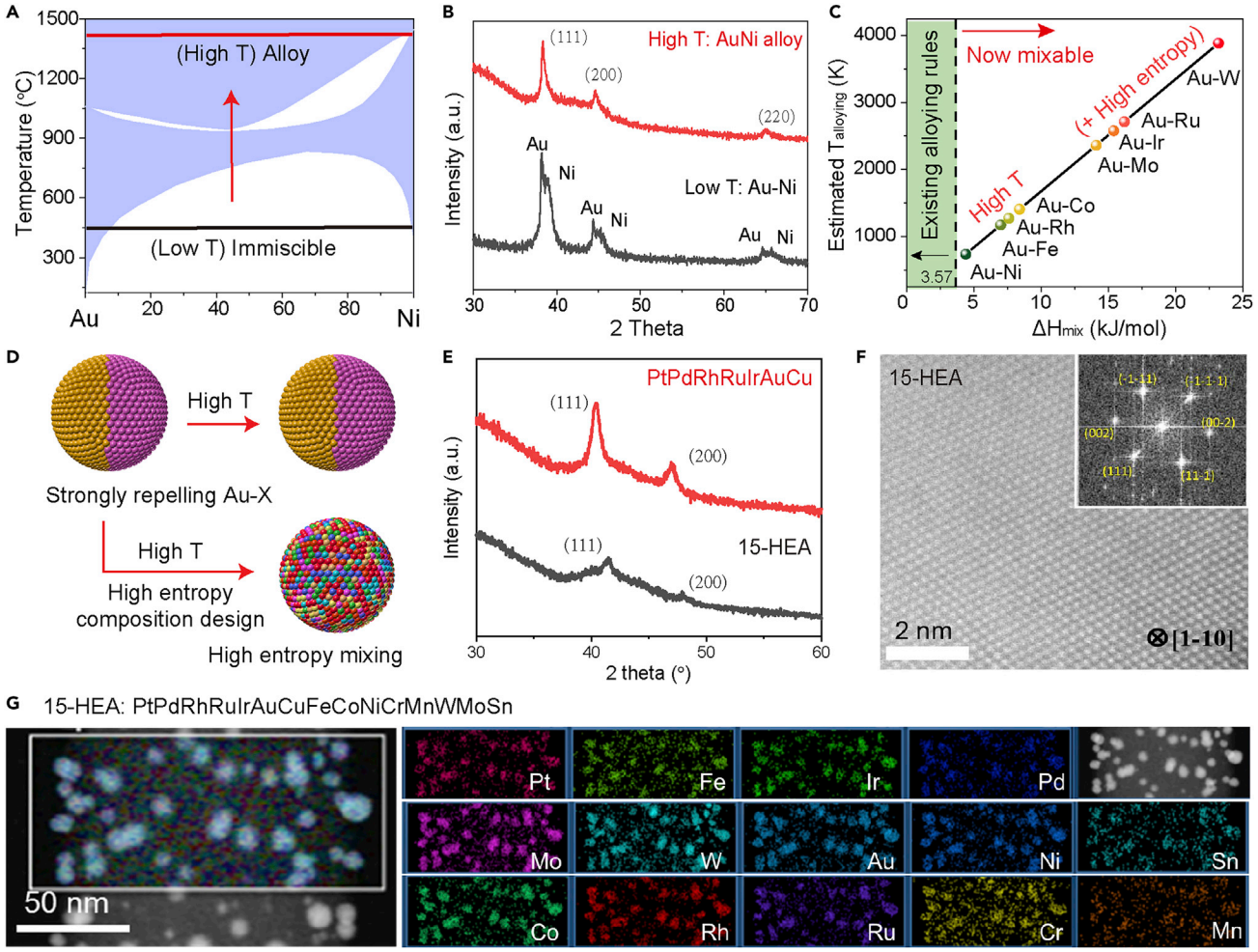

Figure 2. Overcoming immiscibility by high-temperature and high-entropy synthesis

(A) Phase diagram of Au-Ni, showing the immiscible region at low temperature.

(B) XRD profiles of Au-Ni synthesized by high-temperature shock (1,800 K, a single-phase structure) and low-temperature shock (800 K, phase separation of Au and Ni).

(C) Summary of general alloying in Au-based binary combinations. The high-temperature synthesis extends the alloying of elements up to Au-Co, while further extension requires a high-entropy compositional design. The alloying temperature is estimated from $T_{alloying} = \Delta H_{mix}/\Delta S_{mix}$.

(D) Schematic demonstrating the mixing of strongly repelling Au-X combinations with a high-entropy design.

(E) XRD profiles of a 7-element system of noble transition metals and a 15-HEA formulation; both samples show a single-phase structure despite containing strongly repelling combinations.

(F) Atomic-resolution HAADF image of a 15-HEA nanoparticle showing an FCC pattern (inset).

(G) Low-magnification element maps for 15-HEA nanoparticles, showing uniform mixing of early and late transition metals.

See also Figures S1–S4.

XRD as well as transmission electron microscopy (TEM) energy-dispersive X-ray spectroscopy (EDS) mapping (Figures 2B and S2). However, for combinations that are strongly repelling, like Au-Ru and Au-W (ΔH_{mix} > 10 kJ/mol), we still observe phase separation in these binary compositions despite using high-temperature synthesis (Figure S2B).

We hypothesized that increasing the mixing entropy could further increase the entropic contribution in free energy to counterbalance the large mixing enthalpy, which should enable alloy formation in systems that are strongly repelling (Figure 2D). As an example, we applied high-temperature shock to a 7-element system

of noble metals (PtPdRuRhIrAuCu) and observed single-phase mixing as revealed by the XRD profile (Figure 2E), indicating alloying of repelling Au-Ir and Au-Ru. By further increasing the mixing entropy, we synthesized a high-entropy alloy system composed of PtPdRhRuIrAuCuFeCoNiCrMnWMoSn (denoted 15-HEA nanoalloy) uniformly dispersed on the carbon substrates (TEM images in Figure S3). This alloy contains many immiscible combinations and still shows a single-phase structure (Figure 2E), although the diffraction peaks are broadened due to the lattice mismatch among these 15 elements. A high-resolution high-angle annular dark-field scanning electron microscopy (HAADF-STEM) image of a 15-HEA nanoparticle illustrates a crystalline structure with an FCC pattern, proving the material's single-phase structure at the nanoscale (Figure 2F). In addition to the particle-level elemental maps in Figure 1D, we show a low-magnification mapping of the 15-HEA sample, in which all the elements are homogeneously mixed in the nanoparticles (Figure 2G). We also confirmed the homogeneous mixing of these elements by using a Ni based TEM grid (Figure S4).

The uniform alloying among these strongly repelling combinations (e.g., Au-Mo, Au-W) showcases the power of using the increased entropic design ($T^*\Delta S_{mix}$) to overcome the immiscibility and achieve extreme mixing. Although our synthesis is conducted in Au-based combinations, this proof of concept demonstrates the feasibility of extending the enthalpy limit of alloying by a high-temperature and high-entropy strategy, which should be generally applicable to other systems as well.

Entropic contribution to induce metal reduction and stabilization

Another critical issue for nanoscale alloying is a tendency toward oxidation. For high-temperature metal reduction, an Ellingham diagram[33,34] (Figure 3A), which illustrates the oxidation potential ($\Delta G_{oxidation}$) of different elements and the relative ease of reducing an oxide, is often used in metallurgy. Typically, elements on the top have a smaller oxidation potential and their oxides can be reduced by the metallic elements below them. In particular, carbon is ubiquitously used as a high-temperature reducing regent through the carbothermal reduction ($xC + MO_x \xrightarrow{\text{high } T} M + xCO\uparrow$) for elements above the carbon oxidation line (i.e., green line in Figure 3A).[33–36] Note that the Ellingham diagram is summarized for bulk materials with 1 atom O_2 partial pressure, which largely deviates from our nanoscale materials and synthesis in an inert Ar atmosphere. Therefore, the Ellingham diagram only acts as a guideline for the relative oxide potentials of different elements.

In our synthesis, as carbon substrates are employed for Joule heating and high-temperature synthesis, they also serve as natural reducing agents for elements above the carbon oxidation line. To verify the nanoscale carbothermal reduction (CTR), we synthesized Mo nanoparticles under three different conditions: (1) high-temperature CTR (1800 K, 50 ms); (2) low-temperature CTR (800 K, 50 ms three times); and (3) high-temperature heating on an oxide substrate (SiO_2, 1,800 K, 1 s). The X-ray photoelectron spectroscopy (XPS) profiles (Figure 3B) clearly show that Mo is metallic under high-temperature CTR, while low-temperature synthesis or a lack of carbon could lead to a mixture of metallic and oxidized Mo states. We also verified the high-temperature CTR in Co, W, and Hf, where Co and W (above carbon) can be successfully made into metallic nanoparticles, while Hf remains oxidized (Figure 3C). As illustrated in Figure 3D, at nanoscale, noble elements (e.g., Pt) are easily reducible at high temperature; transition elements above carbon can be reduced by our high-temperature CTR method (e.g., Co, W, Mo), while those deep oxides below carbon will remain in oxidized states (e.g., Hf, Zr) due to their high oxidation potentials (Figure S5).

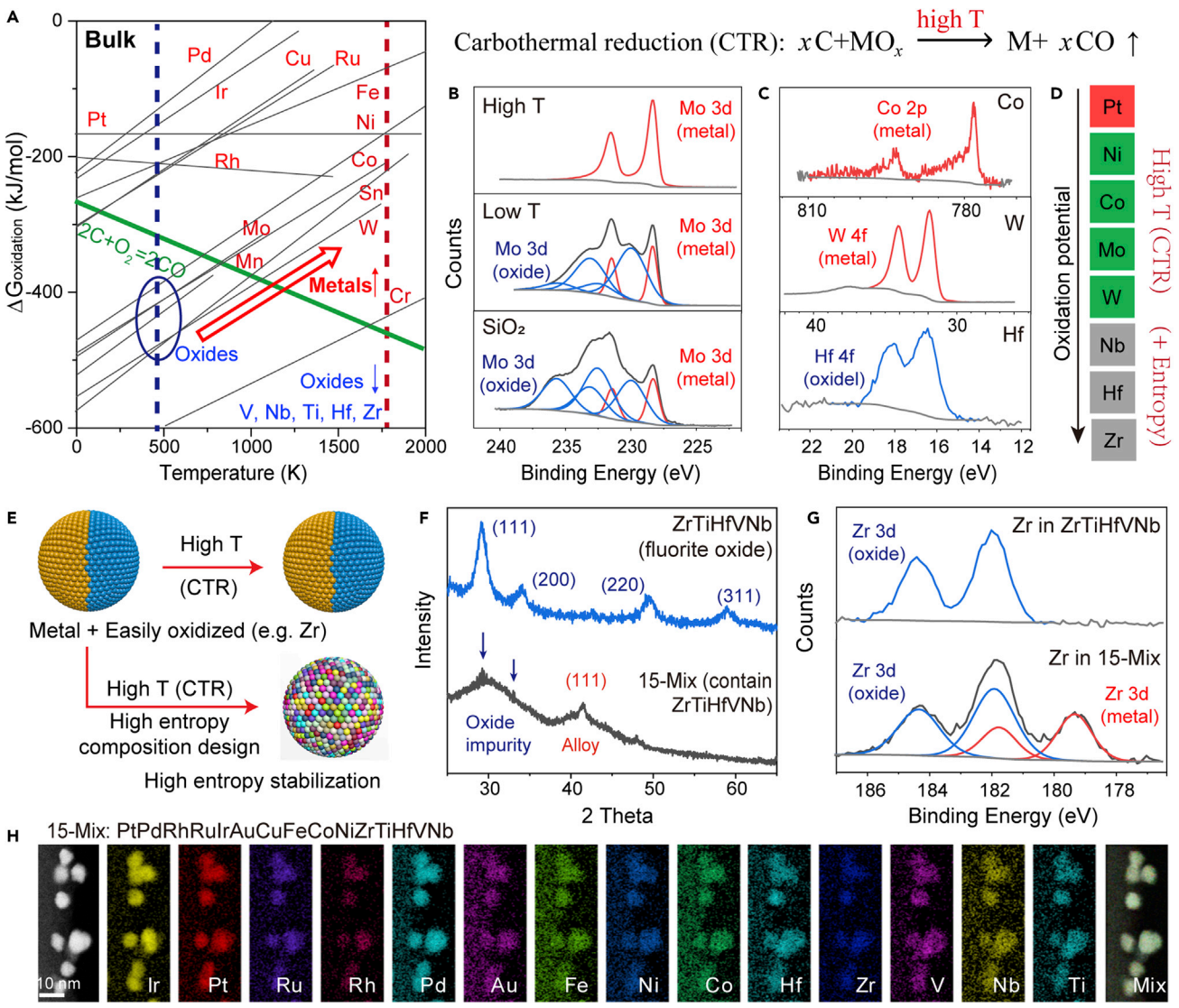

Figure 3. High-temperature- and high-entropy-induced metal reduction

(A) Ellingham diagram[37,38] showing the elemental oxidation potentials and relative ease of metal reduction (bulk materials, 1 atom partial pressure O_2). The elements above the carbon oxidation line ($2C + O_2 \rightarrow 2CO\uparrow$) can be reduced by CTR synthesis.

(B) XPS profiles of Mo nanoparticles synthesized (in Ar atmosphere) by high-temperature CTR (High T), low-temperature CTR (Low T), and high-temperature heating on an oxide substrate (SiO_2). High-temperature CTR is the only method to achieve metallic Mo at the nanoscale.

(C) XPS profiles of Co, W, and Hf synthesized by high-temperature CTR, where Co and W are metallic while Hf is oxidized.

(D) List of nanoscale transition metal reduction by high-temperature CTR synthesis.

(E) Illustration of easily oxidized element stabilized by combining with a high-entropy compositional design.

(F) XRD profiles of ZrTiHfVNb (single-phase fluorite oxide) and 15-Mix (a mixture of metallic FCC with oxide residue).

(G) XPS profiles of Zr in ZrTiHfVNb (completely oxidized) and Zr in 15-Mix (metallic Zr and oxidized Zr). Specifically, the higher entropy converts part of Zr and stabilizes it into a metallic alloy.

(H) STEM elemental maps of 15-Mix, showing incorporation of ZrTiHfVNb elements in the metallic alloy nanoparticles (Cu not mapped).

See also Figures S5–S7.

For those deep oxides, considering that high entropy strongly favors alloy mixing, we hypothesize that by combining high-temperature CTR and high-entropy design, the unique high-entropy structure could thermodynamically and kinetically stabilize these deep oxide elements into the metallic alloys (Figure 3E). We therefore increased the system entropy to a 15-element system to form PtPdRhRuIrAuCuFeCoNiZrTiHfVNb

(denoted 15-Mix). The XRD profile of 15-Mix shows a weak metallic FCC structure with some oxide impurity peaks, and these impurity peaks are similar to a fluorite structure formed by (ZrTiHfVNb)O_x (Figure 3F). The XPS result clearly reveals a mixture of metallic Zr and oxidized Zr in the 15-Mix sample, illustrating that a part of element Zr can be successfully incorporated into the 15-Mix system as metallic state (Figure 3G). This contrasts with the Zr element in ZrTiHfVNb where Zr is completely oxidized (Figure 3G) and verifies our hypothesis that a high-entropy structure could easily stabilize the oxide elements into metallic alloys thermodynamically and kinetically. We also confirmed the metal reduction effect of elements Hf and Nb in the 15-Mix sample as compared with them being complete oxides in a low-entropy configuration (Figure S6). STEM EDS maps further illustrate the elemental distribution in 15-Mix, where ZrTiHfVNb elements were found partially incorporated in the metallic alloy (Figure 3H). At a larger scale, we also revealed the mixture structure of metallic alloy and oxide impurities in 15-Mix (Figure S7). Therefore, while high temperature can induce carbothermic reduction to avoid oxidation, the high-entropy design is critical in stabilizing these elements by kinetically or physically confining them inside the alloy structure away from oxidation.

Detailed characterization of entropy-stabilized nanoalloys

All of the above alloys are achieved by overcoming immiscibility and inducing metal reduction, leading to extreme mixing with unique entropy-stabilized nanostructures. Macroscopically, synchrotron XRD (λ = 0.2113 Å) was used to characterize the 15-HEA nanoparticles because it provides better structural resolution than conventional XRD. As shown in Figure 4A, the majority of the diffraction peaks can be indexed using an FCC packing with a unit cell size of 3.78 Å. The single-phase FCC packing is mostly a composition effect, as most elements in the 15 HEA nanoparticles favor FCC structure in their individual metals. Other structures, such body-centered-cubic, could be achieved if those refractory elements could be alloyed into HEA nanoparticles.[39] Compared with the typical synchrotron profile of simple metals,[40] the diffraction peaks overall are broader, particularly for high-angle peaks, which may be due to the small particle size and the extremely disordered structure among the 15 largely different elements.

We also examined the bonding structures of the 15-HEA nanoparticles using X-ray absorption spectroscopy (XAS) for elements (PdRhRuIrCuFeNiWMoCrMnSn) and their respective metal foils as reference (Figures S8 and S9). Notably, the Fourier-transformed extended X-ray absorption fine structures (FT-EXAFS) profiles representing Ir, Ru, Fe, and W—from the 3d, 4d, and 5d elements in the 15-HEA alloy—all show a similar metallic bonding distance around 2 Å with slight variations in peak position, confirming a uniform alloy bonding with local fluctuations or short-range ordering[26,41,42] (Figure 4B). This contrasts with their corresponding metal foils showing drastically different bonding configurations. The similarity in the metal bonding for different elements in the 15-HEA alloys illustrates the homogeneous distribution of metal elements and a uniform alloy structure without obvious metal segregations. The synchrotron XRD and XAS results, therefore, confirm an alloy structure and uniform bonding environment in 15-HEA nanoparticles at a macroscopic scale with high resolution.

Microscopically, we used a state-of-the-art four-dimensional (4D)-STEM technique[43–46] to observe the detailed structure and local strain behavior in the 15-HEA nanoparticles. In 4D-STEM, an electron probe is rastered across a selected region of interest (two-dimensional [2D] real space), and at each probe position a diffraction pattern is acquired (2D reciprocal space). From these diffraction patterns, local structural information, such as strain and lattice distortions, is

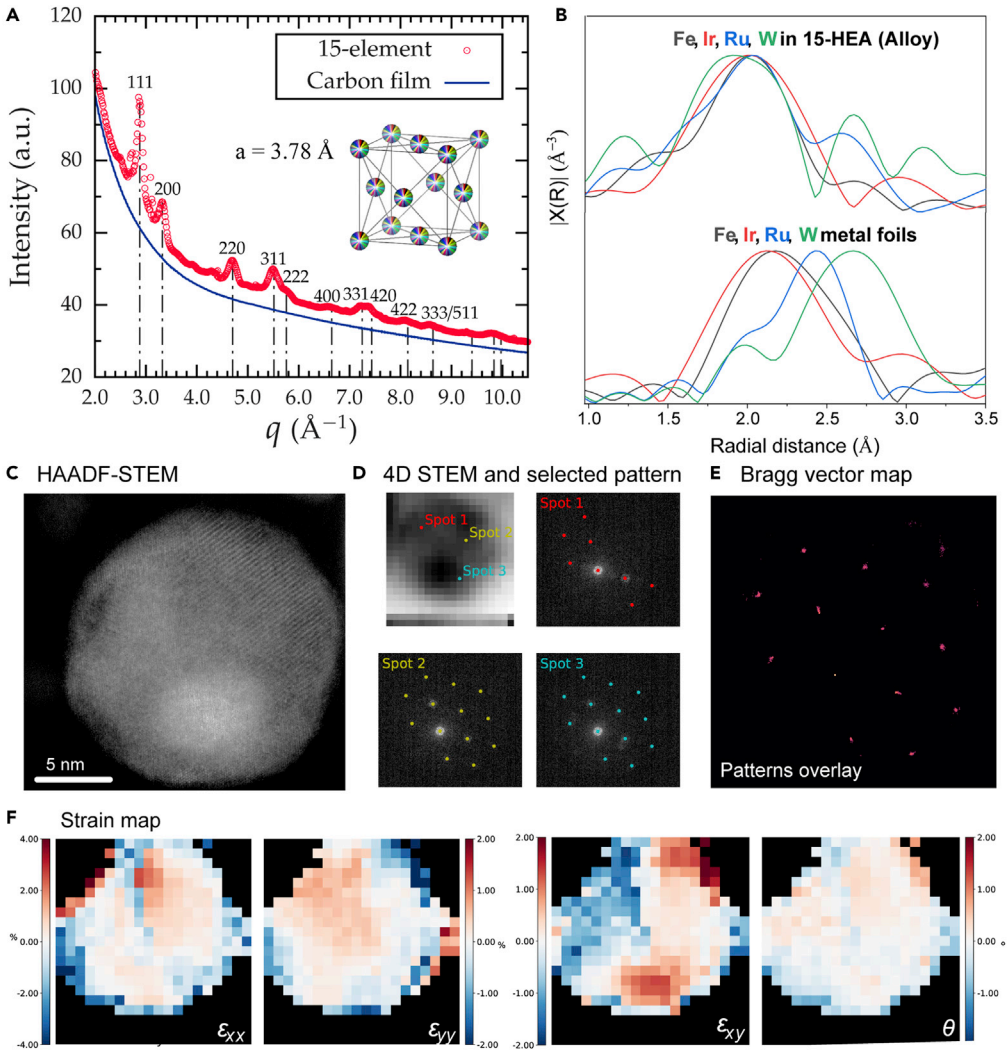

Figure 4. Detailed structural study of the 15-HEA nanoparticles

(A) Macroscopic synchrotron XRD of the 15-HEA nanoparticles, showing an overall single-phase FCC structure.

(B) FT-EXAFS profiles of Fe, Ir, Ru, and W measured in the 15-HEA nanoparticles and comparison with their corresponding pure metal foils, suggesting alloy formation due to the variation in peak position.

(C) High-magnification HAADF-STEM image of a 15-HEA nanoparticle, on which a 4D-STEM dataset of this particle was acquired.

(D) Subsequently generated virtual ADF image in which each pixel corresponds to a diffraction pattern. Three selected diffraction patterns at various locations within this particle are shown.

(E) Bragg vector map showing overlay of all diffraction patterns within the particle.

(F) Strain map of the 15-HEA nanoparticle calculated from the variation in the lattice, showing the localized strain and inhomogeneity in the nanoparticle due to extreme mixing.

See also Figures S8–S11.

determined. Figure 4C shows an atomically resolved HAADF-STEM image of a singular 15-HEA nanoparticle, and a 4D-STEM dataset of this particle was acquired. As demonstrated in Figure 4D, each pixel of the virtual annular dark-field (ADF) image corresponds to a diffraction pattern. Three selected diffraction patterns at different locations within the particle are shown, from which the local structure (lattice constant and strain deformation) are derived. The resulting Bragg vector map (an average deconvolution of all acquired diffraction patterns) indicates the nanoparticle is single crystalline with FCC structure at the single-particle level (Figure 4E).

Localized strain information was calculated using this map as well as the individual diffraction patterns acquired at each point (Figure 4F). The strain maps are calculated according to the variation within individual diffraction patterns as they compare with the average Bragg vector map. Thus, 0% strain change indicates that these regions are comparable with the average Bragg vector map. The step size used is 1 nm/pixel, therefore significant shifts in strain (from tensile to compression) are confined to approximately one to two pixels within the particle (~1–2 nm). As an aside, the bright contrast within the HAADF-STEM image of the nanoparticle is assumed to be a secondary particle, owing to the secondary diffraction pattern observed in Spot 3. It appears to us that the second particle does not disrupt the lattice columns of the primary particle and does not have diffraction patterns indicative of a grain boundary. We therefore assume it is an attachment rather than being inside the primary particle. This secondary particle was excluded from the overall strain map by determining the secondary diffraction pattern and creating a mask for these disks.

The generated strain map of this singular nanoparticle demonstrates strain inhomogeneity, as both tensile (red) and compression (blue) strain are observed. From EDS data of this same region (Figure S10), there does not appear to be chemical inhomogeneity. The changes in strain do correlate with changes in the atomic lattice observed in the atomic-resolution HAADF-STEM image (Figure 4C). We observe that the majority of the strain inhomogeneity, a sharp pixel-to-pixel change from compression to tension or low strain to high strain, is confined to the edges of the particle as well as the boundaries between the changes in atomic lattice fringes. Excluding these rapid changes, the variation of strain within the particle is less than $\pm$0.5%, which is likely related to short-range ordering and distortions due to the extreme mixing of 15 elements with differing crystal structures. This observation indicates that although HEA nanoparticles overall are in a single-phase structure, they are not completely random or uniform; rather, there are natural composition and structure fluctuations (e.g., short-range ordering) leading to local heterogeneity within the materials and causing localized strain and lattice distortions.[41,44,47]

Despite these localized strains and distortions, we confirmed that 15-HEA nanoparticles are thermally stable by *in situ* heating in the TEM chamber up to 600°C (Figure S11). Both the size distribution and alloy structure exhibited no obvious change during the *in situ* heating process (isothermal holding for at least 30 min). The thermal and structural stability may come from the entropy stabilization effect, whereby a high-entropy structure is stabilized both thermodynamically ($\Delta G_{mix} = \Delta H_{mix} - T\Delta S_{mix}$) and kinetically (sluggish diffusion due to large distortions).[16,28,30,42] The 4D-STEM result in particular clearly illustrated strain and distortions in the lattice of entropy-stabilized 15-HEA nanoparticles, which could serve as local diffusion barriers for phase separation and therefore improve the structural stability. Additionally the strain inside the nanoparticles could largely tune the performance, especially for catalysis.[26,48]

DISCUSSION

To summarize our synthesis strategy, we plotted the transition metal alloying guided by the mixing enthalpy and oxidation potentials as a reference (Figure 5A). Conventionally, easily mixed alloys are found under restrictive conditions with a mild mixing enthalpy (e.g., $\Delta H_{mix} < 3.57$ kJ/mol) and easily reducible elements (e.g., $\Delta G_{oxidation} > -300$ kJ/mol). To extend the alloy spaces, we used extreme entropic contribution ($-T^*\Delta S_{mix}$) to drive alloy formation, for example,

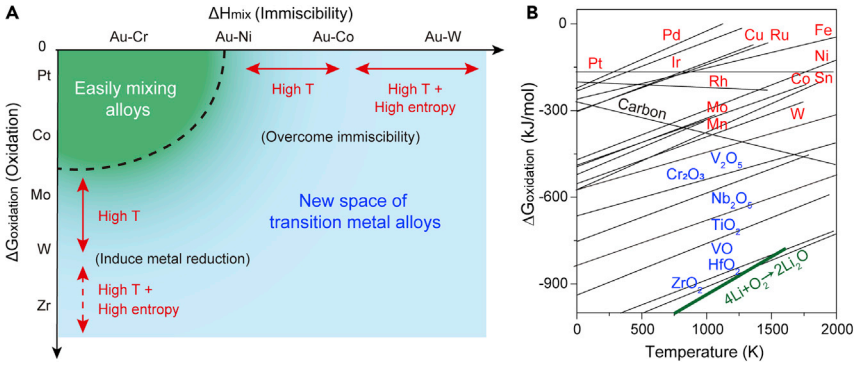

Figure 5. Strategies for extending the metallic alloying spaces at the nanoscale

(A) Extended alloy space of transition metals at the nanoscale by overcoming immiscibility and inducing metal reduction. In these processes, high temperature and high entropy are critical to driving the alloy formation in a large range of immiscibility (x axis) and oxidation potentials (y axis). The solid arrow indicates metallic alloys formed in the range, while the dashed arrow indicates partial metal reduction and stabilization.

(B) Ellingham diagram with more easily oxidized elements included. Notably, lithium is at the lowest position and can reduce the elements above the lithiothermic reduction line to achieve metallic alloys with these easily oxidized elements.

See also Figure S12 and Note S1.

high-temperature 1,800 K synthesis combined with a 15-element high-entropy design. As demonstrated, the limiting enthalpy was elevated to Au-Co (~10 kJ/mol) by high-temperature synthesis and further to Au-W (~25 kJ/mol) by combining with high-entropy-driven mixing, which could cover all the possible binary combinations in the transition metal space.[10] Additionally, using the Ellingham diagram as a guide, our high-temperature synthesis induced carbothermal reduction to convert transition elements (e.g. Ni, Mo, W) into metallic nanoparticles, including some partial refractory metals (e.g., Zr), by high-entropy compositional design. Therefore, our entropically driven synthesis largely extends the alloy spectrum in transition metals by overcoming the immiscibility and inducing metal reduction, enabling a vast space for alloy exploration that is full of potential for broad applications.

In addition, it is noteworthy that there are still deep oxide transition metals (mostly refractory metals) that have not been made into nanoscale alloys. Inspired by nanoscale carbothermal reduction, we propose that these easily oxidized elements can be reduced to the metallic alloy by nanoscale metallothermic reduction.[35,36,49,50] As illustrated in Figure 5B, lithium has the lowest oxidation potential and therefore highest reduction capability through the lithiothermic reduction reaction ($2xLi + MO_x \xrightarrow{high\ T} M + xLi_2O$).[51] We presented some preliminary data on the lithiothermic reduction of refractory metals at the nanoscale, showing XRD and electrochemical tests suggesting potential metal reduction (Figure S12 and Note S1); however, the metals are easily oxidized when exposed again in the air. Further reduction and stabilization strategies would be a promising direction to take to extend alloying toward those easily oxidized elements at the nanoscale.

Lastly, in this paper the extreme mixing in our 15-element nanoalloy highlights the capability of alloying strongly immiscible combinations and easily oxidized elements. Compared with the number of mixes, the types of the constituent elements are more important in gaining qualification as an extreme mixing alloy. In our design, high entropy benefits alloy formation thermodynamically and kinetically. From a

thermodynamic point of view, high entropy naturally favors a random mixing structure (i.e., alloy formation) based on the Gibbs free energy consideration ($\Delta G_{mix} = \Delta H_{mix} - T^*\Delta S_{mix}$), whereby the increase in the entropy (also the temperature) will largely decrease the mixing Gibbs free energy and therefore drive alloy formation. From a kinetic point of view, high-entropy structure features a random mixing of many different elements, which can cause large lattice distortions and strain inhomogeneity inside the particle. The distorted structures can also "trap" or "freeze" the mixing structure inherited from the high-temperature synthesis due to difficulties in atom diffusion and structure relaxation. It should be noted that besides entropy considerations, other physicochemical properties will also affect the single-phase mixing, for example, atom size mismatch, valence electron concentration, and the size effect.[52] Therefore, the entropy-driven strategy acts as an important methodology and descriptor for alloy mixing, yet the precise evaluation of each contributing parameter will require more experiments and perhaps a data-driven discovery process.[15,17]

Conclusion

In this paper, we explored an entropic design strategy ($-T^*\Delta S_{mix}$) for single-phase alloy formation at the nanoscale among transition metal elements—specifically, how different elements can be successfully incorporated into an alloy structure and what the potential alloying capabilities are. By systematic synthesis and exploration of many alloy nanoparticles, we found that the mixing enthalpy (implication of immiscibility) and Ellingham diagram (implication of oxidation potential) are critical guidelines for structure prediction. By following the alloying guidelines, we have used the high-temperature and high-entropy design to achieve record-high 15-element HEA nanoparticles by overcoming immiscibility in strongly repelling combinations and inducing metal reduction for easily oxidized elements. These unique alloy nanoparticles demonstrate overall uniform mixing with localized strain and distortions, which may be a unique characteristic of the extreme mixing of so many dissimilar elements. Our synthesis largely expands the spectrum of possible transition metal alloys and enables a range of previously inaccessible elemental combinations and alloy structures. This vast compositional space is also intriguing for future data-driven material discovery and broad technological applications.

EXPERIMENTAL PROCEDURES

Resource availability

Lead contact

Further information and requests for resources and materials should be directed to and will be fulfilled by the lead contact, Liangbing Hu (binghu@umd.com).

Materials availability

All materials generated in this study will be made available on reasonable request.

Data and code availability

The acquired datasets were analyzed using py4DSTEM, an open-source Python program available on Github (https://github.com/py4dstem/py4DSTEM).

High-temperature shock process

The high-temperature shock synthesis was performed through Joule heating of precursor-loaded carbon nanofiber films in an argon-filled glovebox, similar to the method reported previously.[5] On brief, individual metal salts or their hydrate forms (Sigma-Aldrich) were dissolved in ethanol at a concentration of 0.05 mol/L. The alloy precursors were mixed in the solution phase at a 1:1 molar ratio and loaded

onto a carbon nanofiber film using a pipette with a loading of 5 μmol/cm^2. The high-temperature synthesis was triggered by electric Joule heating using a Keithley 2425 SourceMeter. The shock temperature and duration was tuned by the input electrical power, which we monitored in-line with a home-made high-speed video system.[53]

Structural characterization

The microstructure was characterized by a scanning electron microscope (Hitachi SU-70 FEG-SEM at 10 kV) and transmission electron microscopes (JEOL 2100F FEG TEM/STEM operated at 200 kV, and JEOL TEM/STEM ARM 200CF). The elemental distribution and maps were measured using an Oxford X-max 100TLE windowless X-ray detector. XRD was performed using a D8 Advanced (Bruker AXS, WI, USA) with a scan rate of 3°/min. XPS was performed on Kratos Axis 165 spectrometer. Synchrotron XRD experiments were carried out at the 11-ID-B beamline of the Advanced Photon Source at Argonne National Laboratory (Chicago, IL, USA). The X-ray wavelength was 0.2113 Å, and the sample-to-detector distance was 175.1 mm. Reduction of 2D diffraction patterns to 1D profiles, as well as diffraction peak indexing and Rietveld refinement, were performed using GSAS-II software.

X-ray absorption spectroscopy measurement and analysis

XAS data were collected from the CLS@APS (Sector 20-BM) beamline at the Advanced Photon Source (operating at 7.0 GeV) at Argonne National Laboratory. The sample was measured in fluorescence mode simultaneously with a reference for each element at room temperature and ambient pressure, protected from exposure with oxygen using a sealed aluminum pouch. EXAFS data were normalized and transformed into k-space and R-space using the Athena program with conventional procedures. The k-range used to generate the FT-EXAFS spectra for each element was as follows: 3.0–9.3 Å^{-1} for Cr, 2.3–11.8 Å^{-1} for Cu, 2.2–10.0 Å^{-1} for Fe, 2.5–9.3 Å^{-1} for Ir, 2.4–8.9 Å^{-1} for Mn, 2.2–11.9 Å^{-1} for Mo, 2.2–10.3 Å^{-1} for Ni, 2.3–11.9 Å^{-1} for Pd, 2.0–11.8 Å^{-1} for Rh, 2.1–11.7 Å^{-1} for Ru, 2.9–11.7 Å^{-1} for Sn, and 3.1–12.0 Å^{-1} for W. A k-weighting of 2 was used for each element except for Mn, which used a k-weighting of 1.

Fast scanning electron microscopy

4D-STEM datasets were acquired with a Gatan Orius 830 CCD using an FEI TitanX operated at 300 kV with a beam size of 2 nm and a probe semi-convergence angle of 0.48 mrad. The acquired datasets were subsequently analyzed using py4DSTEM, an open-source Python program available on Github (https://github.com/py4dstem/py4DSTEM).

SUPPLEMENTAL INFORMATION

Supplemental information can be found online at https://doi.org/10.1016/j.matt.2021.04.014.

ACKNOWLEDGMENTS

This work at the University of Maryland is supported by the National Science Foundation (NSF) Scalable Nano-manufacturing project no. 1635221. R.S.-Y.'s and Z.H.'s microscopy efforts were supported by NSF award no. DMR-1809439. L.A.H. and B.H.S. were supported by the Toyota Research Institute. S.E.Z. is supported by STROBE, an NSF Science and Technology Center under grant no. DMR 1548924. Work at the Molecular Foundry was supported by the Office of Science, Office of Basic Energy Sciences of the US Department of Energy (DOE) under contract no. DE-AC02-05CH11231. This work used resources of the Advanced Photon Source,

an Office of Science User Facility operated for the US DOE Office of Science by Argonne National Laboratory and was supported by the US DOE under contract no. DE-AC02- 06CH11357 and the Canadian Light Source and its funding partners. Part of the microscopy work was conducted at the Center for Nanophase Materials Science, which is a US DOE Office of Science User Facility. NIST disclaimer: Certain commercial products or equipment are described in this paper to specify adequately the experimental procedure. In no case does such identification imply recommendation or endorsement by the National Institute of Standards and Technology, nor does it imply that it is necessarily the best available for the purpose.

AUTHOR CONTRIBUTIONS

Conceptualization, L.H. and Y.Y.; Methodology, Y.Y., J.G., T.L., Q.D., and M.J.; Investigation, Y.Y., Z.H., R.S.-Y., L.A.H., S.E.Z., B.H.S., C.O., A.M.M., D.M., Z.F., P.Z., M.C., Y.M., and J.L.; Writing – original draft, L.H. and Y.Y.; Writing – review & editing, all authors; Supervision, L.H.

DECLARATION OF INTERESTS

L.H. is a co-founder of HighT-Tech and a member of its scientific advisory board. All research reported in this paper was performed at the University of Maryland or by collaborators and is the intellectual property of the University of Maryland, not HighT-Tech. HighT-Tech has an exclusive license from the University of Maryland for the commercialization of this type of technology.

Received: August 16, 2020
Revised: February 1, 2021
Accepted: April 15, 2021
Published: May 7, 2021

REFERENCES

1. Greeley, J., Stephens, I.E.L., Bondarenko, A.S., Johansson, T.P., Hansen, H.A., Jaramillo, T.F., Rossmeisl, J., Chorkendorff, I., and Nørskov, J.K. (2009). Alloys of platinum and early transition metals as oxygen reduction electrocatalysts. Nat. Chem. *1*, 552–556. https://doi.org/10.1038/nchem.367.

2. Kluender, E.J., Hedrick, J.L., Brown, K.A., Rao, R., Meckes, B., Du, J.S., Moreau, L.M., Maruyama, B., and Mirkin, C.A. (2019). Catalyst discovery through megalibraries of nanomaterials. Proc. Natl. Acad. Sci. U S A *116*, 40–45. https://doi.org/10.1073/pnas.1815358116.

3. Batchelor, T.A.A., Pedersen, J.K., Winther, S.H., Castelli, I.E., Jacobsen, K.W., and Rossmeisl, J. (2019). High-entropy alloys as a discovery platform for electrocatalysis. Joule *3*, 834–845. https://doi.org/10.1016/j.joule.2018.12.015.

4. Löffler, T., Meyer, H., Savan, A., Wilde, P., Garzón Manjón, A., Chen, Y.-T., Ventosa, E., Scheu, C., Ludwig, A., and Schuhmann, W. (2018). Discovery of a multinary noble metal-free oxygen reduction catalyst. Adv. Energy Mater. *1802269*, 1802269. https://doi.org/10.1002/aenm.201802269.

5. Yao, Y., Huang, Z., Xie, P., Lacey, S.D., Jacob, R.J., Xie, H., Chen, F., Nie, A., Pu, T., Rehwoldt, M., et al. (2018). Carbothermal shock synthesis of high-entropy-alloy nanoparticles. Science *359*, 1489–1494. https://doi.org/10.1126/science.aan5412.

6. Oses, C., Toher, C., and Curtarolo, S. (2020). High-entropy ceramics. Nat. Rev. Mater. *5*, 295–309. https://doi.org/10.1038/s41578-019-0170-8.

7. Chen, P.-C., Liu, M., Du, J.S., Meckes, B., Wang, S., Lin, H., Dravid, V.P., Wolverton, C., and Mirkin, C.A. (2019). Interface and heterostructure design in polyelemental nanoparticles. Science *363*, 959–964. https://doi.org/10.1126/science.aav4302.

8. Chen, P.-C., Liu, X., Hedrick, J.L., Xie, Z., Wang, S., Lin, Q.-Y., Hersam, M.C., Dravid, V.P., and Mirkin, C.A. (2016). Polyelemental nanoparticle libraries. Science *352*, 1565–1569. https://doi.org/10.1126/science.aaf8402.

9. Beaumier, E.P., Pearce, A.J., See, X.Y., and Tonks, I.A. (2019). Modern applications of low-valent early transition metals in synthesis and catalysis. Nat. Rev. Chem. *3*, 15–34. https://doi.org/10.1038/s41570-018-0059-x.

10. Troparevsky, M.C., Morris, J.R., Kent, P.R.C., Lupini, A.R., and Stocks, G.M. (2015). Criteria for predicting the formation of single-phase high-entropy alloys. Phys. Rev. X *5*, 011041. https://doi.org/10.1103/PhysRevX.5.011041.

11. Miracle, D.B., and Senkov, O.N. (2017). A critical review of high entropy alloys and related concepts. Acta Mater. *122*, 448–511. https://doi.org/10.1016/j.actamat.2016.08.081.

12. Ye, Y.F., Wang, Q., Lu, J., Liu, C.T., and Yang, Y. (2016). High-entropy alloy: challenges and prospects. Mater. Today *19*, 349–362. https://doi.org/10.1016/j.mattod.2015.11.026.

13. Hume-Rothery, W. (1969). The structure of metals and alloys. Indian J. Phys. *11*, 74.

14. George, E.P., Raabe, D., and Ritchie, R.O. (2019). High-entropy alloys. Nat. Rev. Mater. *4*, 515–534. https://doi.org/10.1038/s41578-019-0121-4.

15. Islam, N., Huang, W., and Zhuang, H.L. (2018). Machine learning for phase selection in multi-principal element alloys. Comput. Mater. Sci. *150*, 230–235. https://doi.org/10.1016/j.commatsci.2018.04.003.

16. Liu, Z., Lei, Y., Gray, C., and Wang, G. (2015). Examination of solid-solution phase formation rules for high entropy alloys from atomistic Monte Carlo simulations. JOM *67*, 2364–2374. https://doi.org/10.1007/s11837-015-1508-3.

17. Zhou, Z., Zhou, Y., He, Q., Ding, Z., Li, F., and Yang, Y. (2019). Machine learning guided appraisal and exploration of phase design for high entropy alloys. NPJ Comput. Mater. *5*, 128. https://doi.org/10.1038/s41524-019-0265-1.

18. Rost, C.M., Sachet, E., Borman, T., Moballegh, A., Dickey, E.C., Hou, D., Jones, J.L., Curtarolo, S., and Maria, J.-P. (2015). Entropy-stabilized oxides. Nat. Commun. *6*, 8485. https://doi.org/10.1038/ncomms9485.

19. Kwon, S.G., Krylova, G., Phillips, P.J., Klie, R.F., Chattopadhyay, S., Shibata, T., Bunel, E.E., Liu, Y., Prakapenka, V.B., Lee, B., and Shevchenko, E.V. (2015). Heterogeneous nucleation and shape transformation of multicomponent metallic nanostructures. Nat. Mater. *14*, 215–223. https://doi.org/10.1038/nmat4115.

20. Fenton, J.L., Steimle, B.C., and Schaak, R.E. (2018). Tunable intraparticle frameworks for creating complex heterostructured nanoparticle libraries. Science *360*, 513–517. https://doi.org/10.1126/science.aar5597.

21. Liu, Y., Wei, M., Raciti, D., Wang, Y., Hu, P., Park, J.H., Barclay, M., and Wang, C. (2018). Electro-oxidation of ethanol using Pt_3Sn alloy nanoparticles. ACS Catal. *8*, 10931–10937. https://doi.org/10.1021/acscatal.8b03763.

22. Mukaibo, H., Momma, T., and Osaka, T. (2005). Changes of electro-deposited Sn-Ni alloy thin film for lithium ion battery anodes during charge discharge cycling. J. Power Sources *146*, 457–463. https://doi.org/10.1016/j.jpowsour.2005.03.043.

23. Bai, X., Chen, W., Zhao, C., Li, S., Song, Y., Ge, R., Wei, W., and Sun, Y. (2017). Exclusive formation of formic acid from CO_2 electroreduction by a tunable Pd-Sn alloy. Angew. Chem. *129*, 12387–12391. https://doi.org/10.1002/ange.201707098.

24. Wang, D., and Li, Y. (2010). One-pot protocol for Au-based hybrid magnetic nanostructures via a noble-metal-induced reduction process. J. Am. Chem. Soc. *132*, 6280–6281. https://doi.org/10.1021/ja100845v.

25. Lei, Z., Liu, X., Wang, H., Wu, Y., Jiang, S., and Lu, Z. (2019). Development of advanced materials via entropy engineering. Scr. Mater. *165*, 164–169. https://doi.org/10.1016/j.scriptamat.2019.02.015.

26. Wang, L., Zeng, Z., Gao, W., Maxson, T., Raciti, D., Giroux, M., Pan, X., Wang, C., and Greeley, J. (2019). Tunable intrinsic strain in two-dimensional transition metal electrocatalysts. Science *363*, 870–874. https://doi.org/10.1126/science.aat8051.

27. Liu, M., Zhang, Z., Okejiri, F., Yang, S., Zhou, S., and Dai, S. (2019). Entropy-maximized synthesis of multimetallic nanoparticle catalysts via a ultrasonication-assisted wet chemistry method under ambient conditions. Adv. Mater. Interfaces *6*, 1900015. https://doi.org/10.1002/admi.201900015.

28. Tsai, K.Y., Tsai, M.H., and Yeh, J.W. (2013). Sluggish diffusion in Co-Cr-Fe-Mn-Ni high-entropy alloys. Acta Mater. *61*, 4887–4897. https://doi.org/10.1016/j.actamat.2013.04.058.

29. Otto, F., Yang, Y., Bei, H., and George, E.P. (2013). Relative effects of enthalpy and entropy on the phase stability of equiatomic high-entropy alloys. Acta Mater. *61*, 2628–2638. https://doi.org/10.1016/j.actamat.2013.01.042.

30. Murty, B.S., Yeh, J.-W., and Ranganathan, S. (2014). High-Entropy Alloys (Butterworth-Heinemann).

31. Xu, W., Chen, H., Jie, K., Yang, Z., Li, T., and Dai, S. (2019). Entropy-driven mechanochemical synthesis of polymetallic zeolitic imidazolate frameworks for CO_2 fixation. Angew. Chem. Int. Ed. *58*, 5018–5022. https://doi.org/10.1002/anie.201900787.

32. Gao, S., Hao, S., Huang, Z., Yuan, Y., Han, S., Lei, L., Zhang, X., Shahbazian-Yassar, R., and Lu, J. (2020). Synthesis of high-entropy alloy nanoparticles on supports by the fast moving bed pyrolysis. Nat. Commun. *11*. https://doi.org/10.1038/s41467-020-15934-1.

33. Greenwood, N.N., and Earnshaw, A. (2012). Chemistry of the Elements (Elsevier).

34. Reed, T.B. (1971). Free Energy of Formation of Binary Compounds (MIT Press).

35. Okabe, T.H., and Sadoway, D.R. (1998). Metallothermic reduction as an electronically mediated reaction. J. Mater. Res. *13*, 3372–3377. https://doi.org/10.1557/JMR.1998.0459.

36. Xing, Z., Lu, J., and Ji, X. (2018). A brief review of metallothermic reduction reactions for materials preparation. Small Methods *2*, 1800062. https://doi.org/10.1002/smtd.201800062.

37. Chase, M.W., Jr., Curnutt, J.L., Downey, J.R., Jr., McDonald, R.A., Syverud, A.N., and Valenzuela, E.A. (1982). JANAF thermochemical tables, 1982 supplement. J. Phys. Chem. Ref. Data *11*, 695–940.

38. Birks, N., Meier, G.H., and Pettit, F.S. (2006). Introduction to the High Temperature Oxidation of Metals (Cambridge University Press).

39. Senkov, O.N., Miracle, D.B., Chaput, K.J., and Couzinie, J.P. (2018). Development and exploration of refractory high entropy alloys—a review. J. Mater. Res. *33*, 3092–3128. https://doi.org/10.1557/jmr.2018.153.

40. Ingham, B., Hendy, S.C., Fong, D.D., Fuoss, P.H., Eastman, J.A., Lassesson, A., Tee, K.C., Convers, P.Y., Brown, S.A., Ryan, M.P., and Toney, M.F. (2010). Synchrotron X-ray diffraction measurements of strain in metallic nanoparticles with oxide shells. J. Phys. D. Appl. Phys. *43*, 075301. https://doi.org/10.1088/0022-3727/43/7/075301.

41. Ding, Q., Zhang, Y., Chen, X., Fu, X., Chen, D., Chen, S., Gu, L., Wei, F., Bei, H., Gao, Y., et al. (2019). Tuning element distribution, structure and properties by composition in high-entropy alloys. Nature *574*, 223–227. https://doi.org/10.1038/s41586-019-1617-1.

42. Yao, Y., Liu, Z., Xie, P., Huang, Z., Li, T., Morris, D., Finfrock, Z., Zhou, J., Jiao, M., Gao, J., et al. (2020). Computationally aided, entropy-driven synthesis of highly efficient and durable multi-elemental alloy catalysts. Sci. Adv. *6*, eaaz0510. https://doi.org/10.1126/sciadv.aaz0510.

43. Deng, Y., Zhang, R., Pekin, T.C., Gammer, C., Ciston, J., Ercius, P., Ophus, C., Bustillo, K., Song, C., Zhao, S., et al. (2019). Functional materials under stress: in situ TEM observations of structural evolution. Adv. Mater. *1906105*, 1906105. https://doi.org/10.1002/adma.201906105.

44. Zhang, R., Zhao, S., Ophus, C., Deng, Y., Vachhani, S.J., Ozdol, B., Traylor, R., Bustillo, K.C., Morris, J.W., Chrzan, D.C., et al. (2019). Direct imaging of short-range order and its impact on deformation in Ti-6Al. Sci. Adv. *5*, eaax2799. https://doi.org/10.1126/sciadv.aax2799.

45. Zeltmann, S.E., Müller, A., Bustillo, K.C., Savitzky, B., Hughes, L., Minor, A.M., and Ophus, C. (2020). Patterned probes for high precision 4D-STEM Bragg measurements. Ultramicroscopy *209*, 112890. https://doi.org/10.1016/j.ultramic.2019.112890.

46. Ozdol, V.B., Gammer, C., Jin, X.G., Ercius, P., Ophus, C., Ciston, J., and Minor, A.M. (2015). Strain mapping at nanometer resolution using advanced nano-beam electron diffraction. Appl. Phys. Lett. *106*, 253107. https://doi.org/10.1063/1.4922994.

47. Zhang, R., Zhao, S., Ding, J., Chong, Y., Jia, T., Ophus, C., Asta, M., Ritchie, R.O., and Minor, A.M. (2020). Short-range order and its impact on the CrCoNi medium-entropy alloy. Nature *581*, 283–287. https://doi.org/10.1038/s41586-020-2275-z.

48. Luo, M., and Guo, S. (2017). Strain-controlled electrocatalysis on multimetallic nanomaterials. Nat. Rev. Mater. *2*, 17059. https://doi.org/10.1038/natrevmats.2017.59.

49. Wang, N., Huang, K., Hou, J., and Zhu, H. (2012). Preparation of niobium nanoparticles by sodiothermic reduction of Nb2O5 in molten salts. Rare Met. *31*, 621–626. https://doi.org/10.1007/s12598-012-0569-5.

50. Tan, G., Xu, R., Xing, Z., Yuan, Y., Lu, J., Wen, J., Liu, C., Ma, L., Zhan, C., Liu, Q., et al. (2017). Burning lithium in CS_2 for high-performing compact Li_2S-graphene nanocapsules for Li-S batteries. Nat. Energy *2*, 17090. https://doi.org/10.1038/nenergy.2017.90.

51. Yan, J., Zhang, Y., Zhao, Y., Song, J., Xia, S., Liu, S., Yu, J., and Ding, B. (2020). Transformation of oxide ceramic textiles from insulation to conduction at room temperature. Sci. Adv. *6*, eaay8538. https://doi.org/10.1126/sciadv.aay8538.

52. Feng, J., Chen, D., Pikhitsa, P.V., Jung, Y., Yang, J., and Choi, M. (2020). Unconventional alloys confined in nanoparticles: building blocks for new matter. Matter *3*, 1646–1663. https://doi.org/10.1016/j.matt.2020.07.027.

53. Jacob, R.J., Kline, D.J., and Zachariah, M.R. (2018). High speed 2-dimensional temperature measurements of nanothermite composites: probing thermal vs. gas generation effects. J. Appl. Phys. *123*, 115902. https://doi.org/10.1063/1.5021890.

Matter, Volume *4*

Supplemental information

Extreme mixing in nanoscale transition metal alloys

Yonggang Yao, Zhennan Huang, Lauren A. Hughes, Jinlong Gao, Tangyuan Li, David Morris, Steven Eric Zeltmann, Benjamin H. Savitzky, Colin Ophus, Y. Zou Finfrock, Qi Dong, Miaolun Jiao, Yimin Mao, Miaofang Chi, Peng Zhang, Ju Li, Andrew M. Minor, Reza Shahbazian-Yassar, and Liangbing Hu

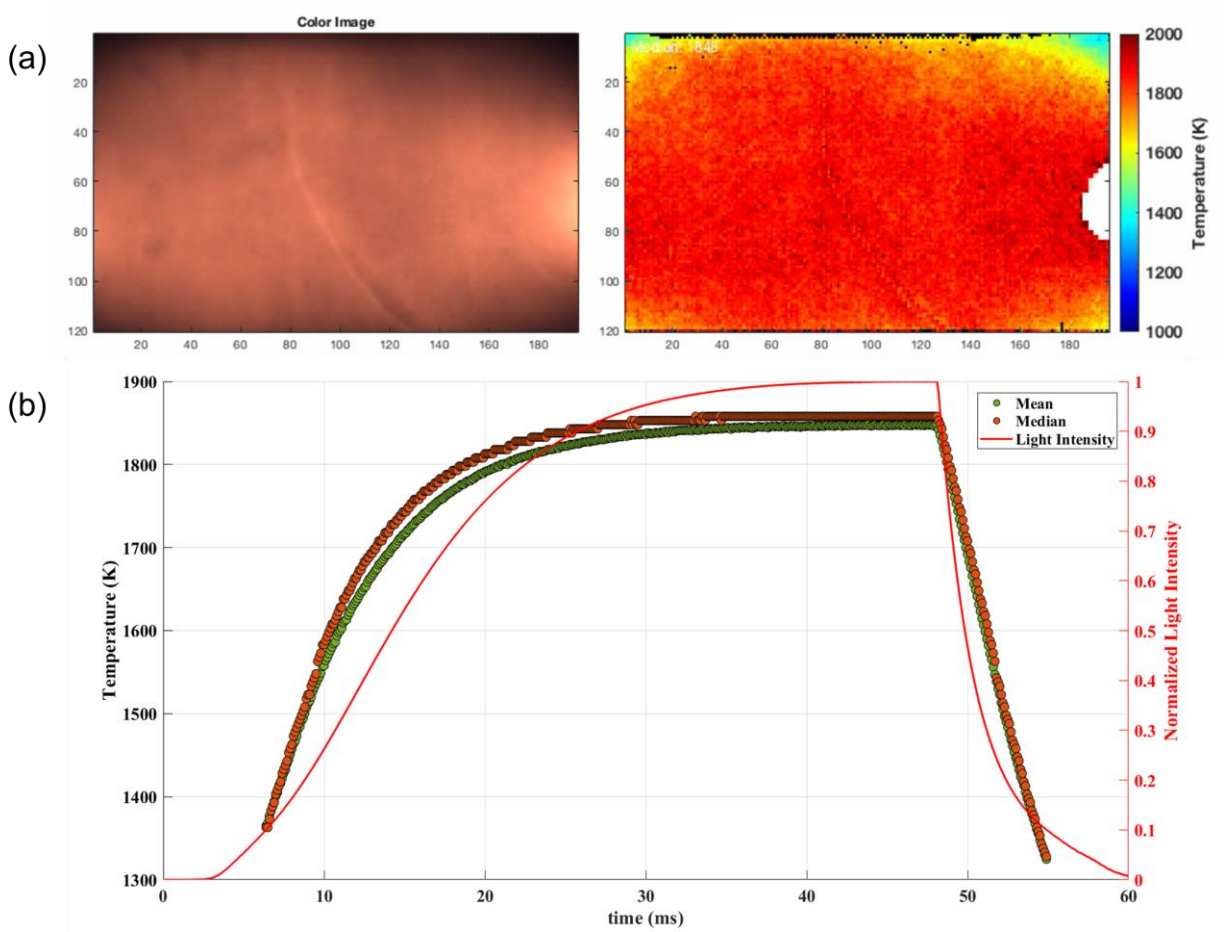

Figure S1. Typical temperature evolution of the high-temperature shock synthesis. (a) An optical image and the corresponding spatial temperature distribution in the AuNi sample loaded on a carbon substrate, demonstrating homogenous heating up to 1800 K. (b) The temperature evolution over time during the thermal shock process, displaying rapid heating and cooling with an overall heating duration of ~50 ms. Related to Figure 2.

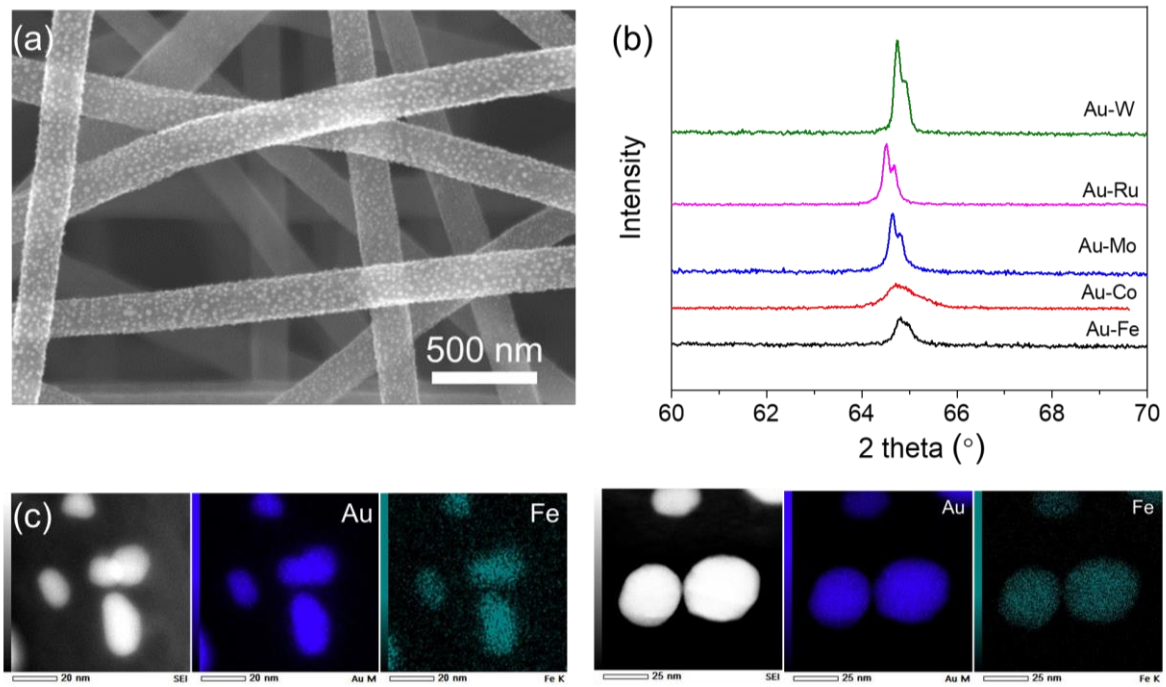

Figure S2. Bimetallic alloy synthesis by high-temperature shock. (a) SEM image of uniformly distributed AuNi alloy nanoparticles synthesized by the high-temperature shock method on a carbon nanofiber substrate. (b) XRD profiles of the Au-based binary alloys synthesized by high-temperature shock, focusing on the (220) peaks in the FCC structure. The Au-Fe and Au-Co samples show an overall FCC structure with a largely broadened peak. However, Au-Mo, Au-Ru, and Au-W materials display a clear phase separation despite the use of high-temperature synthesis. (c) STEM EDS mapping confirming uniform mixing of Au-Fe by our high temperature synthesis. Related to Figure 2.

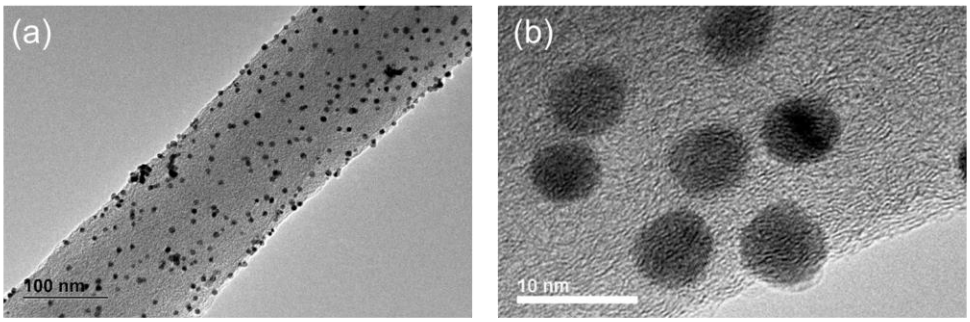

Figure S3. Characterization of the 15-HEA nanoparticles. (a) Low and (b) high magnification TEM images of the 15-HEA nanoparticles dispersed on carbon nanofibers. Related to Figure 2.

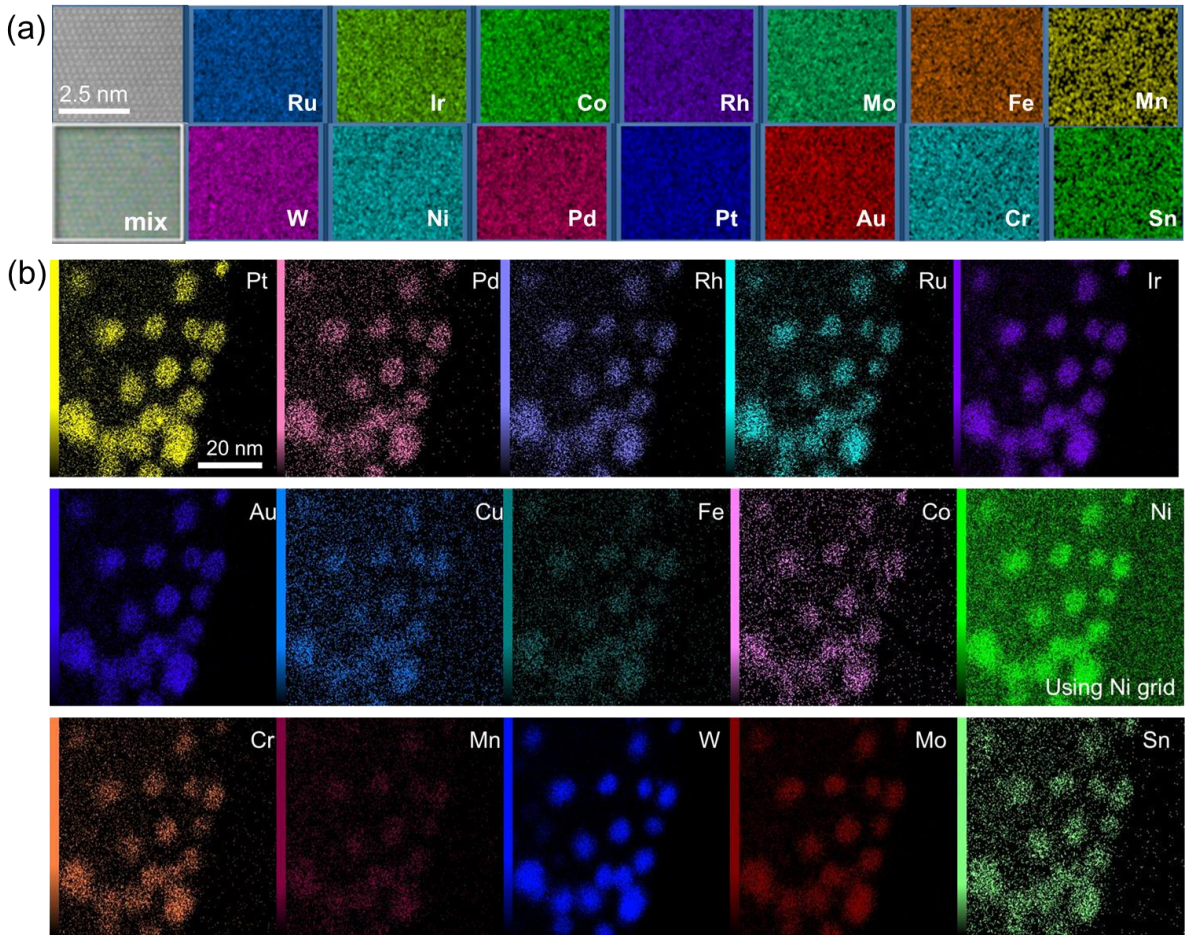

Figure S4. STEM EDS mapping of 15 HEA nanoparticles to show the distribution of different elements: (a) atomic resolution (using Cu grid) and (b) nanoparticles (using a Ni grid). This figure demonstrates the uniform distribution of each element in the alloyed nanoparticles. Related to Figure 2.

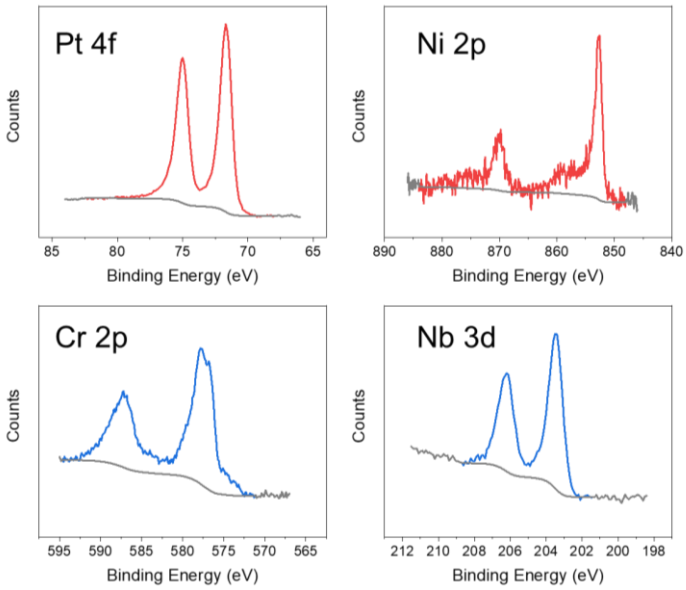

Figure S5. XPS profiles of different transition metal elements by the high-temperature carbothermal reduction synthesis. Pt and Ni are in the metallic state due to high temperature carbothermic reduction, while Cr and Nb are in the oxidized state because of their high oxidation potentials. Related to Figure 3.

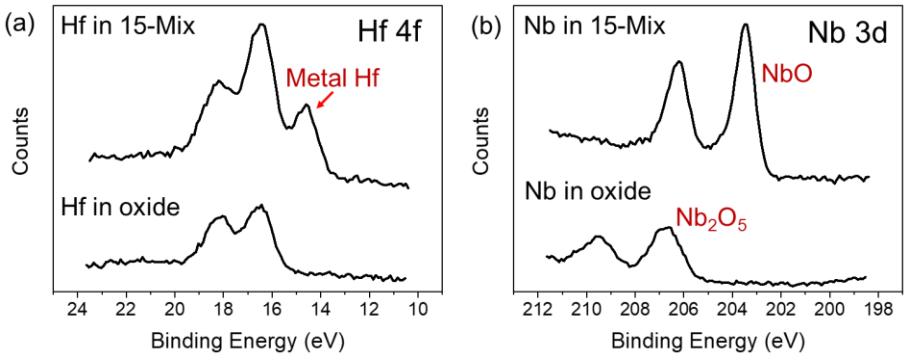

Figure S6. XPS profiles of Hf and Nb in oxides and in 15-Mix sample. The high entropy design in 15-Mix sample evidently improves the metallic composition in Hf and reduced Nb. Related to Figure 3.

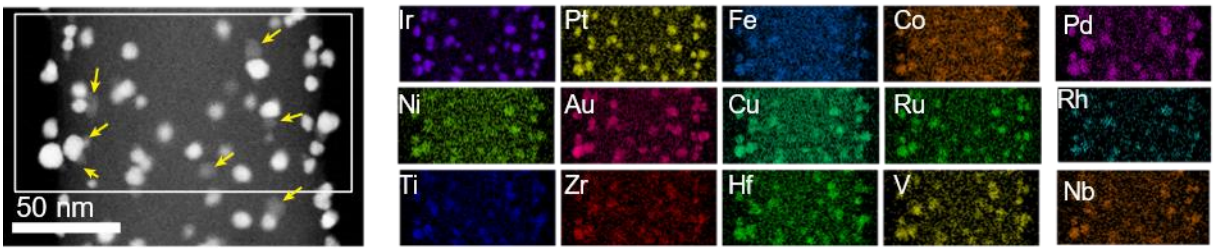

Figure S7. TEM elemental maps of the 15-Mix nanoparticles. Although the high temperature and high entropy design can drive alloy nanoparticle formation, there are still some oxide residues from the easily oxidized elements, mostly ZrTiHfVNb. The different contrasts in the nanoparticles indicate potential oxidized phase (grey, low intensity) while the high intensity particles are generally alloys. The oxides are formed because of direct exposure to ambient environments while these elements frustrated inside the particles can be kept in a metallic state. Related to Figure 3.

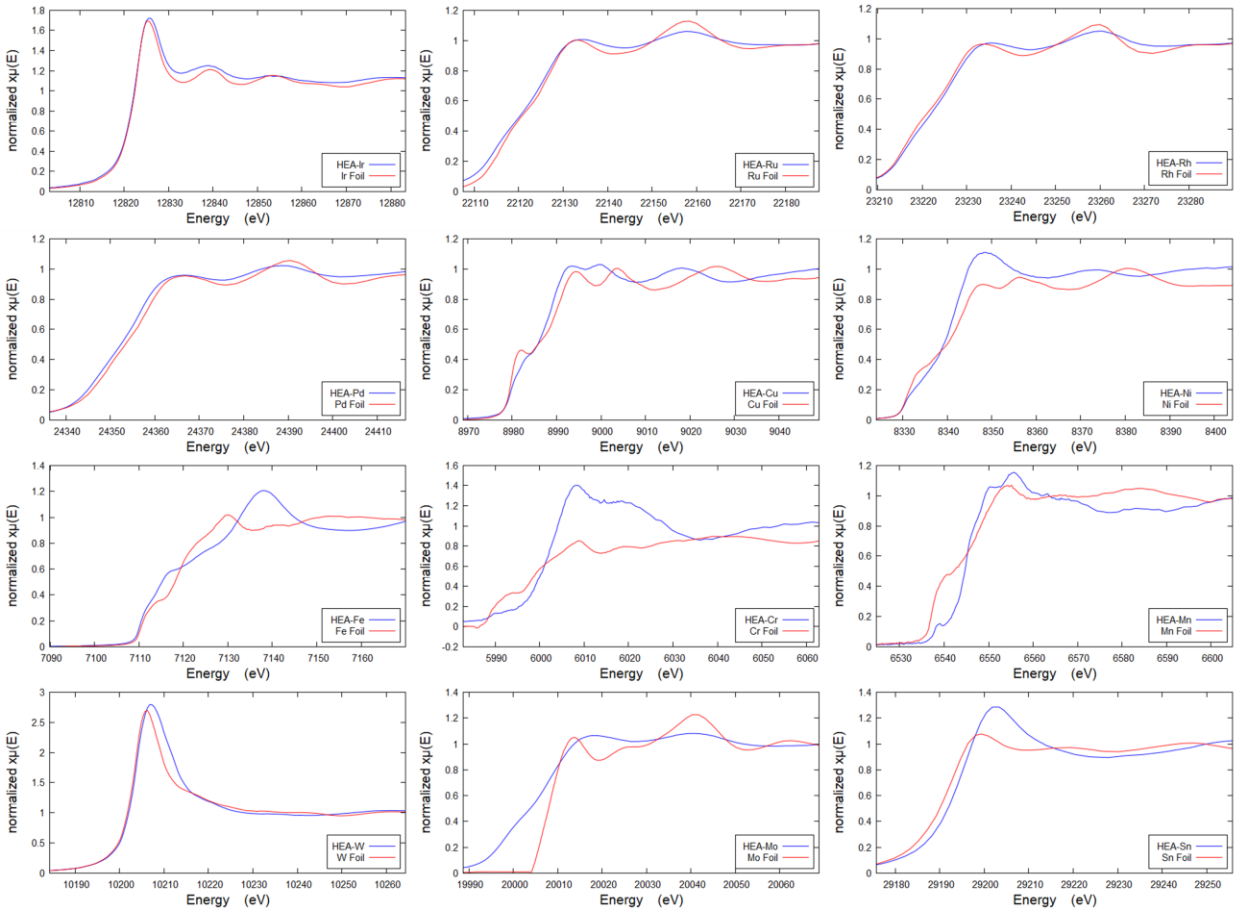

Figure S8. XANES profiles of the 15-HEA nanoparticles, showing that most of the constituent elements are in metallic alloy structures, as indicated by their similarity with reference foils. However, those elements with higher oxidation potentials (e.g., Cr) show an increasing discrepancy with their references, indicating possible oxidation after exposure. Related to Figure 4.

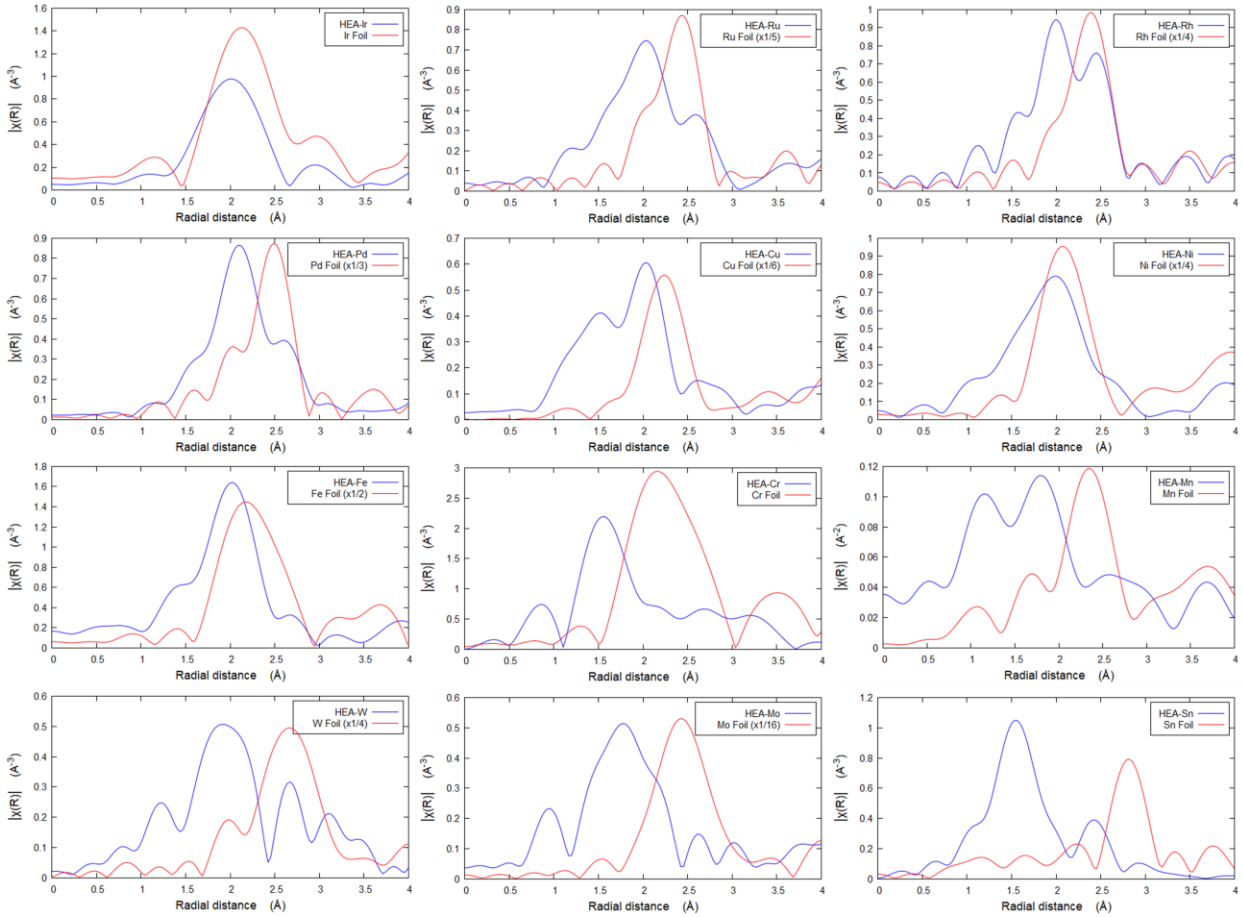

Figure S9. FT-EXAFS spectra of 15-HEA nanoparticles compared with their respective metal foils. Most elements show a peak representing a uniform alloy bonding structure around 2 Å due to alloy formation in the 15-HEA nanoparticles. However, several easily oxidized elements (e.g. Cr, Mn, and Sn) show a major peak at a smaller distance, ~1.5 Å, denoting an oxidized state, which may due to post-oxidation when exposed. Related to Figure 4.

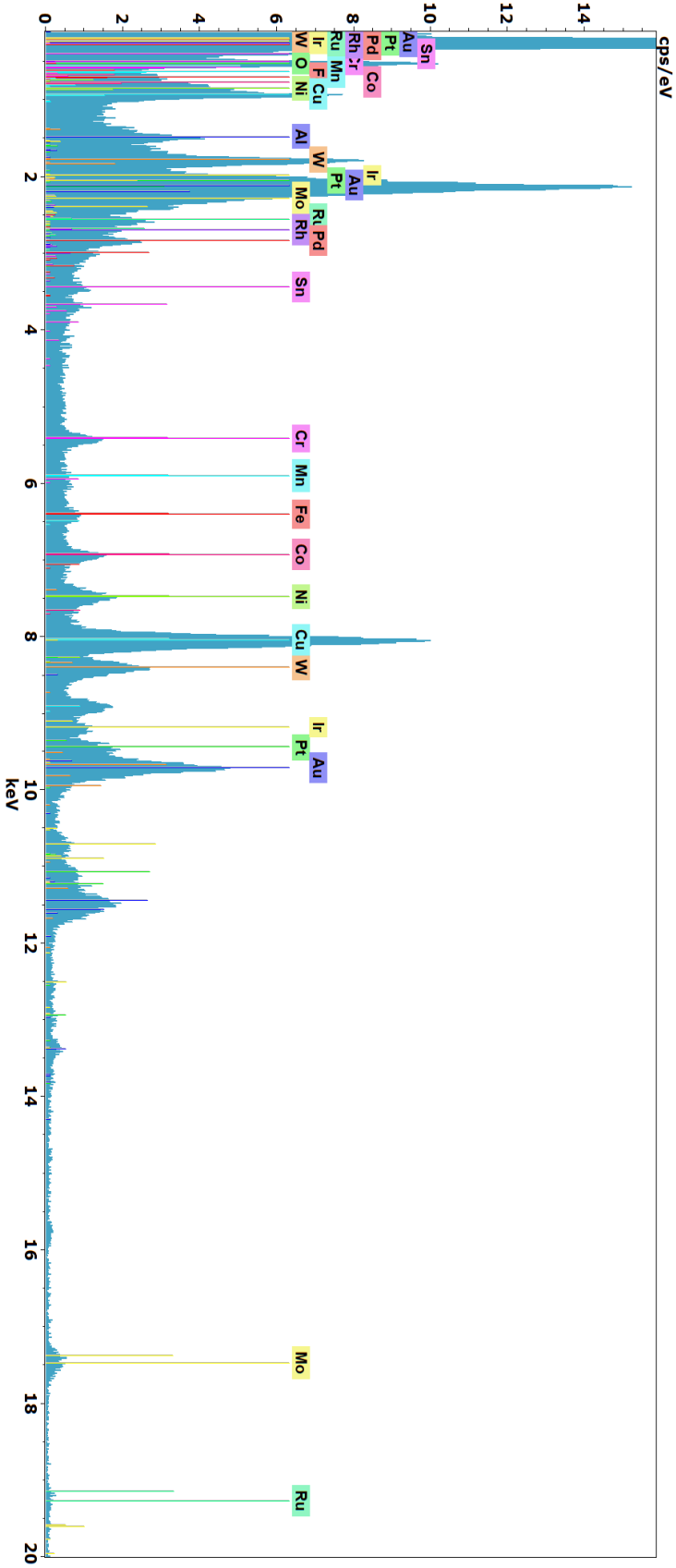

Figure S10: Elemental map spectrum of the 15-HEA nanoparticle used for 4D-STEM characterization, showing the presence of all elements. Related to Figure 4.

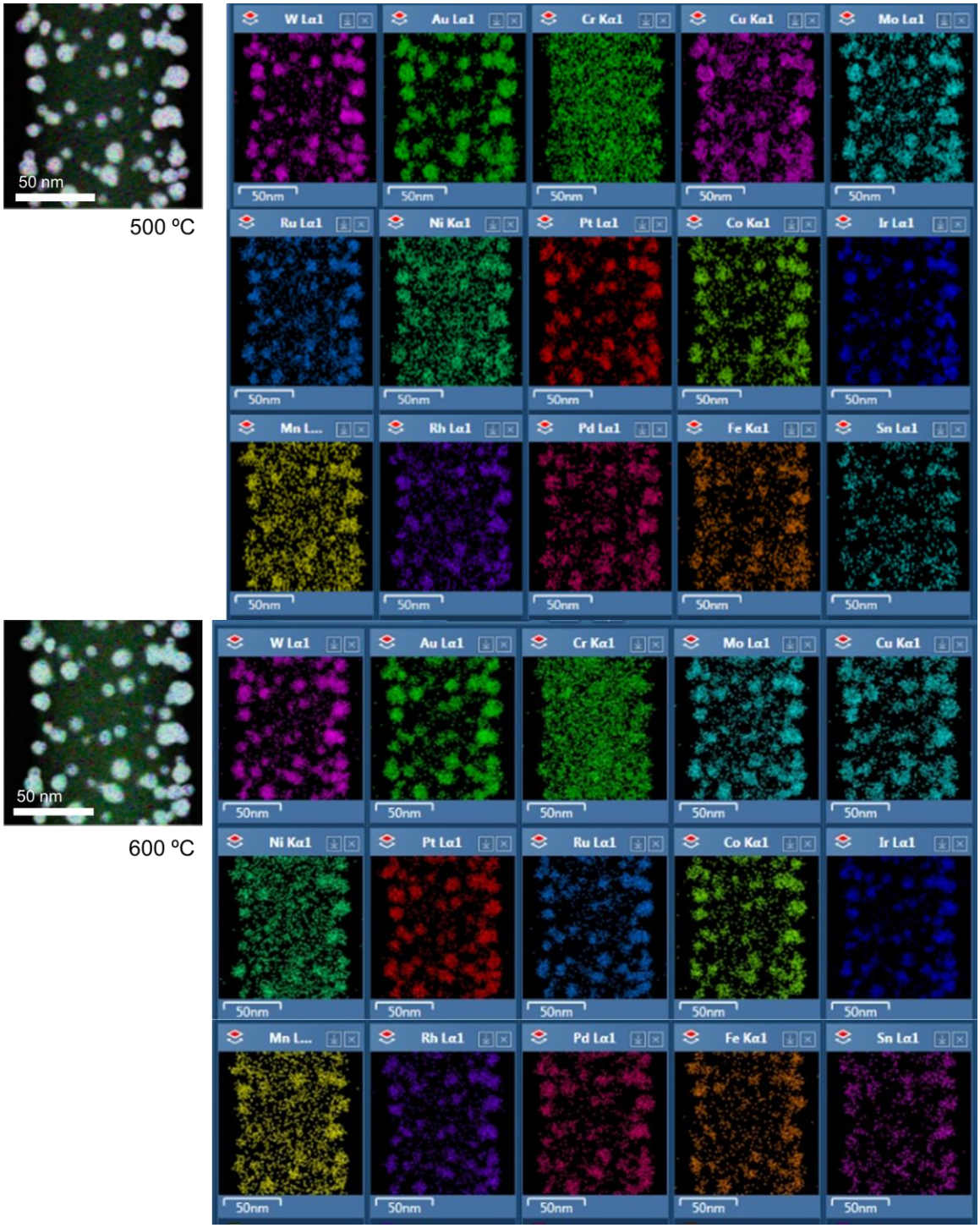

Figure S11. In situ thermal stability of 15-HEA nanoparticles under TEM at 500 ºC and 600 ºC. The sample was maintained at each temperature for at least 30 minutes before taking an image. Related to Figure 4.

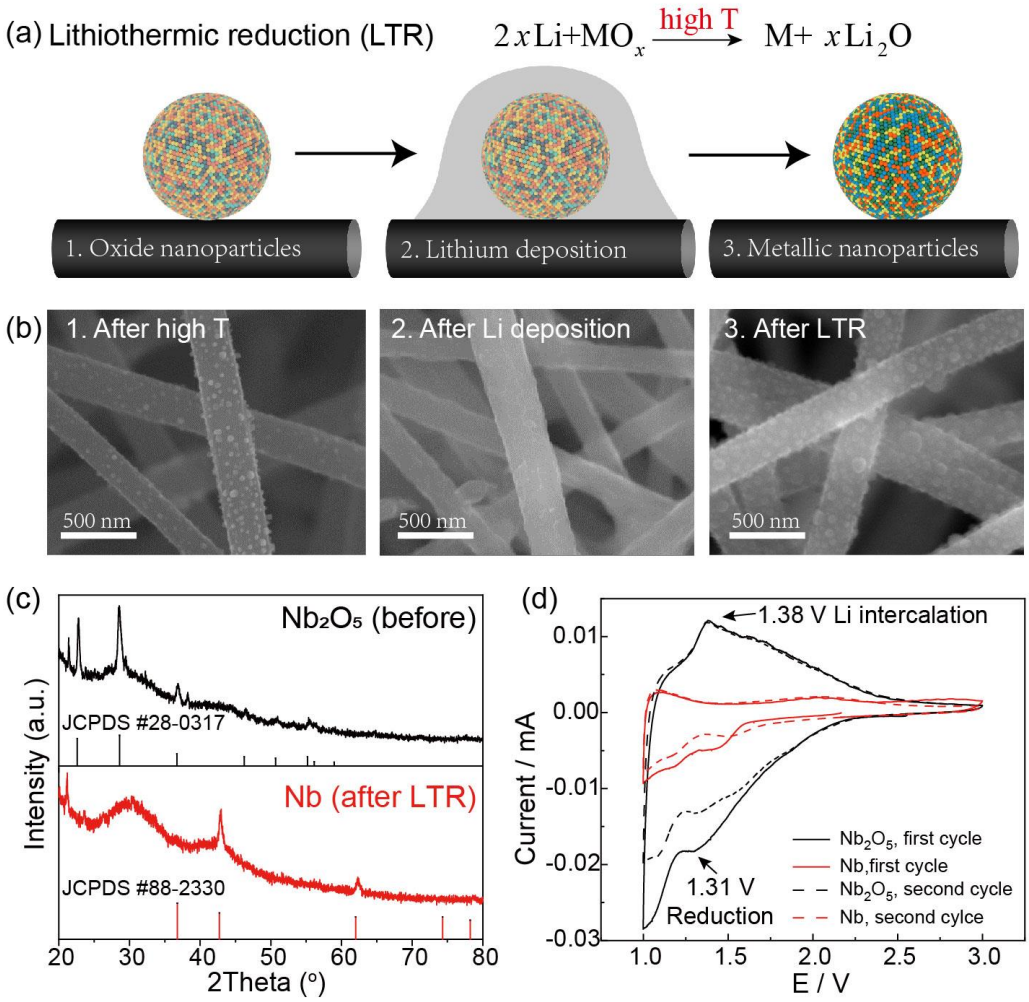

Figure S12. Lithiothermic reduction (LTR) synthesis of metallic nanoparticles. (a) Schematic of the lithiothermic shock process. Step 1, shock synthesis of oxidized nanoparticles dispersed on the carbon substrate; step 2, lithium deposition using an electrochemical lithium-ion cell; and step 3, multiple temperature heating (1000 K, 500 ms, > 20 cycles) to complete the lithiothermic reduction. (b) Corresponding scanning electron microscopy images at each step of the LTR synthesis, showing the morphology evolution of the particles. (c) XRD profile of Nb before and after LTR (sample sealed). The appearance of a peak at ~43° indicates the formation of metallic Nb. (d) The cycle-voltammetry of Nb before and after LTR (in the glovebox). The huge reduction in redox peaks indicates the formation of metallic nanoparticles after the LTR process. Related to Figure 5.

Note S1. Related to Figure 5.
We used multiple thermal shock at relatively low temperature to induce lithiothermic reduction. The key consideration as compared with 1-time carbothermal shock is the low melting temperature and high vapor pressure of lithium. If we use a much higher synthesis temperature (e.g. 1800 K), the lithium can be instantaneously evaporated without having enough time to reduce the oxide nanoparticles (solid reduction reaction/diffusion takes time). At a lower temperature (1000 K), in order to have a complete reaction, we used multiple shock to ensure complete solid state reaction and lithiothermic reduction, which can also help evaporate excess Lithium to expose the nanoparticles.

Table S1. The basic physicochemical properties of transition metal elements and their precursor salts studied in this work. Related to Figure 1.

Precursors	Chemical reduction potential [V]	Metals	Atomic Radius [Å]	Electro-negativity	Melting point [K]	Room-T structure
H_2PtCl_6	0.68, 0.73, 1.18	Pt	1.39	2.28	2041	FCC
$PdCl_2$	0.95	Pd	1.37	2.20	1828	FCC
$RhCl_3$	0.76	Rh	1.34	2.28	2236	FCC
$RuCl_3$	0.45	Ru	1.34	2.2	2527	HCP
$IrCl_3$	1.16	Ir	1.36	2.20	2720	FCC
$FeCl_3$	0.77, -0.44	Fe	1.26	1.83	1811	BCC
$CoCl_2$	-0.28	Co	1.25	1.88	1768	HCP
$NiCl_2$	-0.25	Ni	1.24	1.91	1728	FCC
$HAuCl_4$	1.5	Au	1.44	2.54	1337	FCC
$CuCl_2$	0.34	Cu	1.28	1.90	1358	FCC
$CrCl_3 \cdot 6H_2O$	-0.74	Cr	1.28	1.66	2180	BCC
$MnCl_2$	-1.18	Mn	1.27	1.55	1519	BCC
WCl_6	-0.12	W	1.39	2.36	3695	BCC
$MoCl_5$	-0.15	Mo	1.39	2.16	2896	BCC
$SnCl_2$	-0.14	Sn	1.40	1.96	505	tetragonal
$TiCl_4$	-1.37, -1.63	Ti	1.47	1.54	1941	HCP
$ZrCl_4$	-1.45	Zr	1.60	1.33	2128	HCP
$HfCl_4$	-1.72	Hf	1.59	1.3	2506	HCP
VCl_3	0.34, -0.26, -1.13	V	1.34	1.63	2183	BCC
$NbCl_5$	-1.10	Nb	1.46	1.6	2750	BCC

Reduction potential relative to standard hydrogen electrode;
FCC: face-centered-cubic; BCC: body-centered-cubic; HCP: hexagonal-close-packing.

Table S2. The calculated mixing enthalpy of Au-based binary combinations.[1] Related to Figure 2.

Binary composition	ΔH_{mix} (meV/atom)	ΔH_{mix} (kJ/mol)
Au-Ni	44	4.25
Au-Fe	70	6.75
Au-Rh	76	7.33
Au-Co	84	8.10
Au-Mo	141	13.60
Au-Ir	154	14.86
Au-Ru	162	15.63
Au-W	232	22.38

Supplemental References

1. Troparevsky, M. C., Morris, J. R., Kent, P. R. C., Lupini, A. R. & Stocks, G. M. Criteria for Predicting the Formation of Single-Phase High-Entropy Alloys. *Phys. Rev. X* **5**, 011041 (2015).